Journal of Hazardous Materials 483 (2025) 136669

Contents lists available at ScienceDirect

Journal of Hazardous Materials

journal homepage: www.elsevier.com/locate/jhazmat

Boosting chlorobenzene oxidation over MIL-101(Cr) derived CrO_x catalysts: The stepwise regulation of CrO_x clusters and oxygen species by calcination atmospheres

Boqiong Jiang [a,b], Jun Liu [a], Keyan Wei [a], Hanfeng Lu [c], Xiaole Weng [d], Jingyi Han [a], Yi Zhang [a,b], Shaocai Yu [a], Yuhai Sun [a,b,*]

[a] School of Environmental Science and Engineering, Zhejiang Gongshang University, Hangzhou 310018, China
[b] Zhejiang Province Key Laboratory of Solid Waste Treatment and Recycling, Hangzhou 310012, China
[c] Institute of Catalytic Reaction Engineering, College of Chemical Engineering, Zhejiang University of Technology, Hangzhou 310014, China
[d] College of Environmental and Resource Sciences, Zhejiang University, 310058, Hangzhou, China

HIGHLIGHTS

- The Ar calcination could carbonize the organic ligands of MIL-101(Cr) and prevented the aggregation of CrO_x clusters.
- The coordinative unsaturated Cr^{3+} was retained in Ar and transformed to Cr^{6+} during the treatment of 10 $\%O_2$/Ar.
- Surface OH and Cr^{6+} were important for the activation of chlorobenzene (CB) and the oxidation of the intermediates.
- The surface lattice oxygen could migrate and replenish the oxygen consumed around Cr^{6+} through the oxygen vacancies.
- MIL-101(Cr)-Ar-T showed T90 at 233 °C for the oxidation of CB and high stability with over 95 % selectivity to CO_x and HCl.

GRAPHICAL ABSTRACT

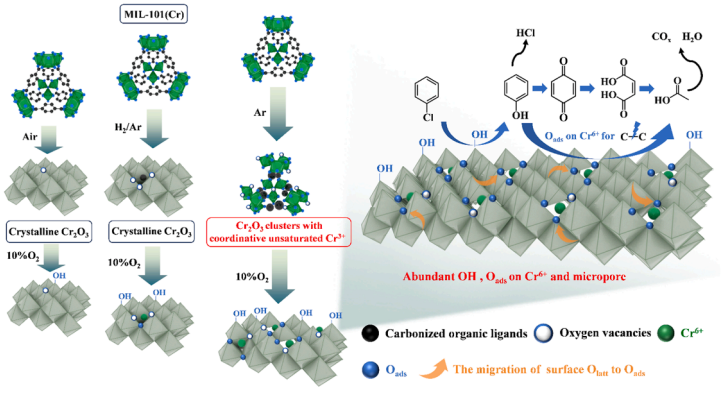

ARTICLE INFO

Keywords:
Calcination atmospheres
CrO_x clusters
Oxygen vacancies
Acid sites
Chlorobenzene catalytic oxidation

ABSTRACT

In this work, CrO_x catalysts derived from MIL-101(Cr) were prepared for the oxidation of chlorobenzene (CB). The atmosphere of calcination had great effect on the physical and chemical properties of the catalysts. Only the atmosphere of Ar could carbonize and preserve the organic ligands in the structure, retaining the micropore structure and high surface area of MIL-101(Cr). Therefore, the aggregation of CrO_x clusters was prevented, forming abundant coordinative unsaturated Cr^{3+} and oxygen vacancies. They would transform to abundant Cr^{6+} as the active sites in the treatment of 10 $\%O_2$/Ar, and acid sites composed with OH and surface adsorbed oxygen were formed around Cr^{6+}, which played an important role on the adsorption/activation of CB and the oxidation of the intermediates. Through the oxygen vacancies, the surface lattice oxygen could migrate and replenish the oxygen consumed around Cr^{6+}. Thus, MIL-101(Cr)-Ar-T, synthesized by MIL-101(Cr) stepwise calcined in Ar and treatment of 10 $\%O_2$/Ar, exhibited the highest catalytic activity for CB oxidation with the T90 at 233 °C, and the

* Corresponding author at: School of Environmental Science and Engineering, Zhejiang Gongshang University, Hangzhou 310018, China.
E-mail address: yhsun@zjgsu.edu.cn (Y. Sun).

https://doi.org/10.1016/j.jhazmat.2024.136669
Received 29 September 2024; Received in revised form 14 November 2024; Accepted 24 November 2024
Available online 26 November 2024

selectivity to CO_x and HCl at 240 °C could reach 95.85 % and 97.61 %, respectively, with a high stable performance in the 5-day catalytic activity test.

1. Introduction

As a waste-to-energy power generation technology, incineration is an important way for municipal solid waste disposal [1]. Besides the emission of particulates, sulfur dioxide and nitrogen oxides, waste incineration also generates chlorinated volatile organic compound (Cl-VOCs), such as chlorobenzene (CB), chlorophenols, polychlorinated dibenzo-p-dioxins and furans (PCDD/Fs), which are widely concerned due to their high toxicity and chemical stability, as well as difficult to degrade [2–4]. Therefore, the removal of Cl-VOCs from incineration flue gas is of great importance to the environment.

Catalytic oxidation technology is considered as an effective method to remove Cl-VOCs [5–8]. Noble metals, such as Pt, Pd, Rh and Ru [9–11], and transition metal oxides like V_2O_5 [12,13], CrO_x [14,15], CeO_2 [16] and MnO_x [17], are used as the active components of the catalysts. Although noble metals show high activity for Cl-VOCs removal, they are easy to be deactivated by the deposition of Cl species, and the high cost also limits the application. Therefore, low-cost transition metal oxide catalysts attract extensive attention. The abundant acid sites on the surface of CrO_x can transform Cl ions to HCl or Cl_2 effectively, which reduce the deposition of Cl on the catalysts, leading to high stability [18]. Furthermore, Cr^{6+} species promote the oxidization of by-products and intermediates [19]. The advantages above make CrO_x more attractive for Cl-VOCs removal. Due to the limitations of active oxygen and Cr^{6+} content, the conventional CrO_x catalysts require a higher oxygen concentration (21 $\%O_2$) and reaction temperature above 300 °C to oxidize Cl-VOCs [14,20]. However, the oxygen concentration of the flue gas from waste incineration is only about 10 % and the operating temperature is below 300 °C in the entire air pollution control devices [21]. Therefore, novel CrO_x catalysts should be explored with high activity under low oxygen concentration and at low-temperature.

In recent years, metal oxides catalysts formed by the calcination of metal-organic frameworks (MOFs) performed high oxidation ability of VOCs at low temperature [22], with more oxygen vacancies on the catalyst surface [23], more acid sites exposure resulted by the rich porous structure and high specific surface area [24]. Among them, MIL-101(Cr) is a MOFs material with Cr as the inorganic metal site. Previous studies have shown that metal oxide catalysts derived from MIL-101(Cr) exhibit high catalytic oxidation activity for VOCs. Chen et al. [25] prepared CrO_x catalyst by calcining MIL-101(Cr) in air, which exhibited more surface adsorbed oxygen than commercial Cr_2O_3, by the transformation of oxygen on oxygen vacancies, and showed T90 at 310 °C when they were used for toluene oxidation. When the oxygen migration was further promoted, the T90 could be reduced to 268 °C [25]. Compared to toluene, the oxidation of Cl-VOCs is more complicated. It includes the break of C-Cl bond, the removal of Cl species, and the oxidation of intermediates, which could accomplish the completely oxidation and avoid the formation of chlorinated byproducts. Both surface acidity and redox ability are important for the deep oxidation of Cl-VOCs [26].

Some research has shown that the calcination atmospheres of MOFs influence the surface acidity, oxygen vacancy content and redox ability of their derived catalysts. For example, Qin et al. [27] prepared FeO_x/C catalysts by calcining MIL-101(Fe) in a CO/N_2 reducing atmosphere and found that CO promoted the exposure of the Fe_3O_4(111) of the catalyst, thereby increasing the surface adsorbed oxygen and surface acidity content. In addition, Zheng et al. [28] found that when Mn-BDC MOF catalysts was calcined in N_2, the dispersion of MnO_x could be improved, and the catalysts exhibited higher acetone oxidation activity due to more oxygen vacancies and higher redox ability compared to those calcined in air, with the T90 decreasing by 13 °C. However, the influence of the calcination atmospheres on CrO_x catalysts derived from MIL-101(Cr) is hardly reported, and the variation in different calcination atmospheres and the effects on Cl-VOCs oxidation are also unknown.

Therefore, in this paper, MIL-101(Cr) was used as the precursor. After calcination in different atmospheres (Air, H_2/Ar and Ar), the catalysts were further treated in 10 $\%O_2$/Ar at 300 °C, and then used for the catalytic oxidation of CB as a typical kind of Cl-VOCs. The influence of different calcination atmospheres on MIL-101(Cr) was characterized by X-ray diffractometer (XRD), Brunauer-Emmett-Teller (BET), Ultraviolet-visible spectrophotometer (UV–vis) and X-ray photoelectron spectrometer (XPS), combined the analysis by using online mass spectrometry (MS). The chemical properties and catalytic performance of the catalysts were characterized by Hydrogen temperature-programmed reduction (H_2-TPR), Cycled hydrogen temperature-programmed reduction (Cycled H_2-TPR), Oxygen temperature-programmed desorption (O_2-TPD), Ammonia temperature-programmed desorption (NH_3-TPD), and Chlorobenzene temperature-programmed desorption (CB-TPD) experiments. Finally, the influence of different calcination atmospheres on the reaction mechanism was investigated by in situ diffuse reflectance infrared Fourier transform spectroscopy (in situ DRIFTs) and density functional theory (DFT) calculations.

2. Experimental

2.1. Chemicals and materials

Cr $(NO_3)_3{\cdot}9H_2O$ (AR, 99 %), terephthalic acid ($HO_2CC_6H_4CO_2H$, AR, 99 %) were purchased from Shanghai Macklin Biochemical Technology Co., Ltd; HF (AR, ≥40 wt%), ammonium hydroxide ($NH_3{\cdot}H_2O$, AR, 25–28 wt%) and ethanol (CH_3CH_2OH, AR, 95 %) were purchased from Shanghai Ling Feng Chemical Reagent Co., Ltd.

2.2. Catalyst preparation

MIL-101(Cr) was prepared using one-step hydrothermal method. The detailed process was provided in the Supporting Information.

0.5 g of MIL-101(Cr) was weighed and calcined at 500 °C for 4 h in Air, 10 $\%H_2$/Ar, and Ar atmospheres, respectively, denoted as MIL-101(Cr)-Air, MIL-101(Cr)-H_2, MIL-101(Cr)-Ar. Before being used for CB oxidation, the catalysts above were treated at 300 °C in 10 $\%O_2$/Ar for 1 h, forming MIL-101(Cr)-Air-T, MIL-101(Cr)-H_2-T, MIL-101(Cr)-Ar-T, respectively.

Additionally, CrO_x was prepared by precipitation method for comparison, denoted as CrO_x-P-T. The detailed process was also provided in the Supporting Information.

2.3. Catalytic test

The oxidation of CB was carried out in a quartz glass tube with 10 mm inner diameter. The reaction tube was filled with 75 mg of catalyst and 0.5 g of quartz sand (40–60 mesh). The total flow rate was 50 mL/min, and the weight hourly space velocity (WHSV) was 40000 mL/(g·h). The reactant feed was consisted of 100 ppm CB, 30 ppm SO_2 (when used), 10 $\%O_2$, balanced by N_2. The composition of the tail gas was measured by an online gas chromatograph (GC 1690, JIEDAO, China) equipped with a flame ionization detector (FID). The CB conversion and CO_x selectivity were calculated using the following equations:

$$\text{CB conversion } (\%) = \frac{([CB]_{in} - [CB]_{out})}{[CB]_{in}} \times 100\% \quad (1)$$

$$\text{Selectivity to CO } (\%) = \frac{[CO]_{out}}{6 \times ([CB]_{in} - [CB]_{out})} \times 100\% \quad (2)$$

$$\text{Selectivity to } CO_2 \quad (\%) = \frac{[CO_2]_{out}}{6 \times ([CB]_{in} - [CB]_{out})} \times 100\% \quad (3)$$

Where in and out represented the inlet and outlet concentration of CB, CO and CO_2, respectively.

The HCl and Cl_2 selectivity were measured by ion chromatograph (Dionex ICS-900, Thermo Fisher, USA) and N, N-diethyl-p-phenylenediamine spectrophotometry (UV-2000, UNICO (Shanghai) Instrument Co., Ltd., China).). The detailed method was also provided in the Supporting Information.

2.4. Catalyst characterization

The crystalline structure of the catalysts (after calcination and after the treatment of 10 %O_2/Ar) was studied by X-ray diffractometer (D8 Advance, Bruker, Germany) with Cu Kα radiation (λ = 1.5418 Å). XRD patterns were collected at 40 kV and 40 mA, scanning 2θ range from 5° to 90° with a step size of 0.02°.

The specific surface area, pore volume, and pore diameter of the catalysts (after calcination and after the treatment of 10 %O_2/Ar) were determined by a physical adsorption analyzer (Micromeritics ASAP 2020 PLUS HD88, Micromeritics, USA). The specific surface area was calculated by the Brunauer-Emmett-Teller (BET) method, and the pore diameter and pore volume were calculated by the Barrett-Joyner-Halenda (BJH) and Hovath-Kawazoe (H-K) methods, respectively.

UV–vis diffuse reflectance spectra were collected by a UV–vis spectrophotometer (Hitachi U-3900, Hitachi, Japan) in absorbance mode with $BaSO_4$ as a reference.

XPS analysis was conducted on an X-ray photoelectron spectrometer (Thermo Fisher Scientific ESCALAB 250Xi, Thermo Fisher Scientific, USA) to detect the surface chemical states and elemental composition of the catalysts (after calcination and after the treatment of 10 %O_2/Ar) using Al Kα (hv = 1486.6 eV) as the excitation source. The binding energy of adsorbed organic contamination carbon, C 1 s = 284.8 eV, was used as a reference for calibration. Corrections were made for spectral line shifts caused by charging effects, and peak fitting was performed to obtain XPS spectra.

The products in tail gas during the calcination and treatment process of the catalysts were studied by a mass spectrometer (Tilon LC-D200M, Ametek, USA) with full scanning and online monitoring modes.

The thermal stability of the catalysts (after the treatment of 10 %O_2/Ar) was studied by Thermogravimetric Analysis (TGA) (Themys one, Setaram, France). The temperature increased from 20 °C to 300 °C at a rate of 10 °C/min and was kept at 300 °C for 4 h under 10 %O_2/He.

H_2-TPR: The catalysts (after calcination) were treated at 300 °C in 10 %O_2/Ar for 1 h, followed by switching to Ar for another 30 min. The temperature was then decreased to 50 °C in Ar atmosphere, followed by purging with 10 %H_2/Ar for 30 min. Subsequently, the temperature was ramped up to 500 °C at a rate of 10 °C/min and hold for 30 min with a gas flow rate of 50 mL/min·H_2O signal was measured online using a mass spectrometer (Tilon LC-D200M, Ametek, USA).

Cycled H_2-TPR: The two kinds of cycled H_2-TPR experimental process were shown in Scheme 1, the gas flow rate was 50 mL/min·H_2O signal was measured online using a mass spectrometer (Tilon LC-D200M, Ametek, USA).

O_2-TPD, NH_3-TPD, CB-TPD: The catalysts (after calcination) were treated at 300 °C in 10 %O_2/Ar for 1 h, then cooled to 50 °C in Ar atmosphere, followed by adsorption of 10 %O_2, 4 % NH_3, 250 ppm CB for 30 min, for O_2-TPD, NH_3-TPD and CB-TPD, respectively. Then the catalyst was purged with Ar until the baseline was stable. After that, the temperature ramped up at 10 °C/min to 800 °C for O_2-TPD and NH_3-TPD, and to 240 °C for CB-TPD, and hold for 30 min with a gas flow rate of 50 mL/min. O_2, NH_3, CB, HCl, Cl_2, CO, and CO_2 in the tail gas was measured online for by a mass spectrometer (Tilon LC-D200M, Ametek,

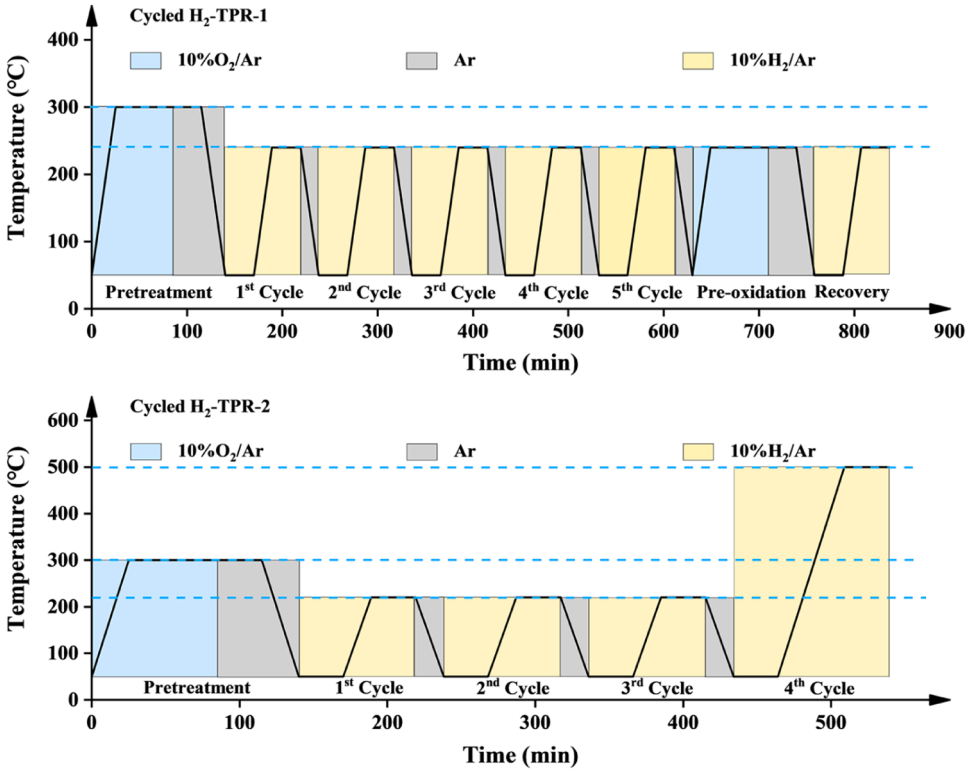

Scheme 1. Cycled H_2-TPR procedure.

USA).

The Electron Paramagnetic Resonance (EPR) was carried out by a spectrometer (Bruker EMXplus, Bruker, Germany) operating at X-band frequency (v≈9.84 GHz), the signals of the catalysts (after the treatment of 10 %O_2/Ar) were recorded at room temperature.

The process of CB catalytic oxidation on the catalyst surface was measured by an in situ diffuse reflectance infrared Fourier transform spectrometer equipped with an MCT-A detector (Nicolet iS50, Thermo Fisher Scientific, USA). The infrared high-temperature reaction cell (HVC-DRP-5, Harrick, USA) was equipped with two ZnSe windows and an observation window. Prior to testing, the catalysts (after calcination) were treated at 300 °C in 10 %O_2/Ar at a flow rate of 50 mL/min for 1 h, then cooled to 240 °C, and background spectra were collected. Subsequently, the reaction proceeded for 60 min in the presence of 400 ppm CB and 10 %O_2 at a total flow rate of 50 mL/min, the spectra were recorded with 32 scans at 4 cm^{-1} resolution.

3. Results and discussion

3.1. The effect of different calcination atmosphere on the catalysts

3.1.1. Crystalline properties

The crystalline structure of the catalysts after calcination and treatment of 10 %O_2/Ar were characterized by XRD, as shown in Fig. 1(A) and (B). MIL-101(Cr) was reported with the structure of CrO_x metal clusters linking with the organic ligands terephthalic acid [29]. After calcination in different atmospheres, XRD patterns of MIL-101(Cr)-Air and MIL-101(Cr)-H_2 showed diffraction peaks at 2θ = 24.6, 33.6, 36.2, 41.6, 50.3, 54.9, 63.5, and 65.2°, corresponding to the (012), (104), (110), (113), (024), (116), (214), and (300) crystal planes of Cr_2O_3 (PDF#82–1484), indicating that CrO_x clusters in MIL-101(Cr) had transformed to the crystalline Cr_2O_3 in the calcination atmospheres of Air and 10 %H_2/Ar. The intensity of diffraction peaks of MIL-101(Cr)-H_2 was lower than MIL-101(Cr)-Air, showing lower crystallinity of Cr_2O_3 in MIL-101(Cr)-H_2. The crystallite size was calculated by Scherrer equation, as shown in Fig. 1(C), with 15.3 and 17.5 nm for MIL-101(Cr)-H_2 and MIL-101(Cr)-Air, respectively. Calcination atmosphere of 10 %H_2/Ar would reduce the Cr in MIL-101(Cr) by inducing the escape of oxygen atom [30], and effectively prevented the formation of crystalline Cr_2O_3 phase and thus obtained a better dispersion of Cr species than the air-calcined catalyst [31]. XRD pattern of MIL-101(Cr)-Ar did not show any diffraction peaks of crystalline Cr_2O_3, only a broad peak was detected, indicating that Cr was well dispersed with low crystallinity, might still in the form of CrO_x clusters.

After the treatment of 10 %O_2/Ar, the XRD pattern of MIL-101(Cr)-Air-T had little variation. It seemed that the Cr_2O_3 formed after calcination in the atmosphere of Air already had a stable crystalline structure. The crystallinity of MIL-101(Cr)-H_2-T increased slightly compared to MIL-101(Cr)-H_2, and the crystallite size also increased slightly from 15.3 nm to 15.8 nm. In contrast to the above two catalysts, there was a significant change on MIL-101(Cr)-Ar after the treatment of 10 %O_2/Ar. MIL-101(Cr)-Ar-T showed diffraction peaks of crystalline Cr_2O_3 with a similar crystallite size with MIL-101(Cr)-Air-T, indicating that CrO_x clusters were oxidized to form crystalline Cr_2O_3 in an oxidation atmosphere. Crystalline Cr_2O_3 was formed during the treatment of 10 %O_2/Ar only in MIL-101(Cr)-Ar-T, whereas the formation took place during the calcination in the other catalysts.

3.1.2. Physical structure

The variation of the specific surface area and pore structure of the catalysts after calcination and treatment of 10 %O_2/Ar were analyzed by N_2 adsorption-desorption, as shown in Fig. 1(D), (E) and Table 1. Fig. S1 showed that MIL-101(Cr) displayed the type I isotherm, and the micropore was with the diameter of 0.4–2 nm. The specific surface area and pore volume of MIL-101(Cr) were 2772.13 m^2/g and 1.4 cm^3/g, respectively. The isotherms of MIL-101(Cr)-Air and MIL-101(Cr)-H_2 became type III with obvious H3 hysteresis loops after calcination, implying the micropore were transformed into mesoporous [32,33], and the specific surface areas decreased to 59.11 m^2/g and 136.32 m^2/g, respectively. The physical structure of MIL-101(Cr) collapsed after the

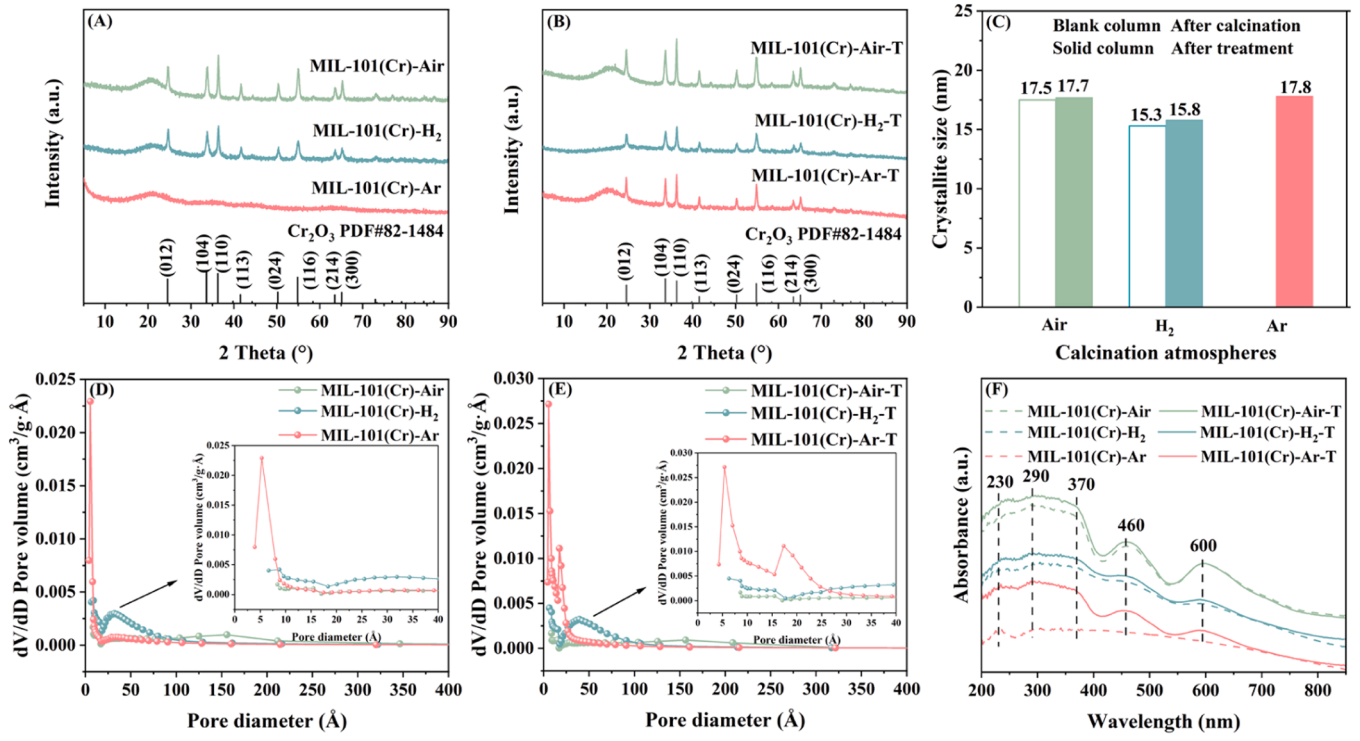

Fig. 1. XRD spectra of the catalysts after (A) calcination and (B) treatment of 10 %O_2/Ar, crystallite size calculated by the Scherrer equation (C), pore diameter distribution of the catalysts after (D) calcination and (E) treatment of 10 %O_2/Ar, UV–vis spectra of the catalysts after calcination and treatment of 10 %O_2/Ar (F).

Table 1
The surface area, pore volume and pore diameter of different catalysts.

Catalysts	BET (m^2/g)	Pore volume (cm^3/g)	Average pore diameter (nm)
MIL−101(Cr)	2772.13	1.40	2.02
MIL−101(Cr)-Air	59.11	0.26	17.36
MIL−101(Cr)-H_2	136.32	0.17	5.13
MIL−101(Cr)-Ar	223.07	0.14	2.44
MIL−101(Cr)-Air-T	55.72	0.19	13.74
MIL−101(Cr)-H_2-T	137.34	0.20	5.88
MIL−101(Cr)-Ar-T	357.61	0.22	2.48

calcination in the atmosphere of Air and 10 %H_2/Ar, and it was more serious in Air. Different from the two catalysts above, MIL-101(Cr)-Ar still displayed the type I isotherm. Although there was also some collapse of the micropores, some micropores still retained with the same diameter (0.4–2 nm) as in MIL-101(Cr), indicating that the atmosphere of Ar was beneficial to retain the physical structure of MOF during the calcination process. The specific surface area of MIL-101(Cr)-Ar was 223.07 m^2/g, much higher than other two catalysts.

After treatment of 10 %O_2/Ar, the specific surface areas of MIL-101 (Cr)-Air-T and MIL-101(Cr)-H_2-T remained almost unchanged, proving that these two catalysts had reached a relatively stable state during the calcination process. However, MIL-101(Cr)-Ar-T underwent a considerable structural change, and the specific surface area increased from 223.07 m^2/g to 357.61 m^2/g. Meanwhile, the pore volume increased by 1.5 times compared to MIL-101(Cr)-Ar, with a little increase of pore diameter from 2.44 to 2.48 nm. Part of micropores were with the diameter of 0.4–2 nm, indicating that part of the physical structure of MIL-101(Cr) was maintained after treatment of 10 %O_2/Ar. The kinetic diameters of CB and oxygen were 0.619 nm and 0.346 nm, respectively, which were much smaller than the average pore diameter of MIL-101 (Cr)-Ar-T. Therefore, the high specific surface area and micropore structure could promote the exposure of Cr species on the catalyst surface, enhancing their exposure to CB, and then promote the oxidation of CB [34–36].

3.1.3. UV–vis diffuse reflectance spectroscopy study

It was generally believed that the form of Cr was an important factor influencing the catalytic oxidation of VOCs [37,38]. The coordination environment of surface Cr in catalysts after calcination and treatment of 10 %O_2/Ar was analyzed by UV–vis diffuse reflectance spectra, as shown in Fig. 1(F). The peaks in the range of 200–400 nm were assigned to the Cr^{6+} resulted from the isolated chromium oxide with a tetrahedral symmetry [37,39]; the peaks at 460 nm and 600 nm were corresponded to the typical octahedral symmetry of Cr^{3+} species (such as crystalline Cr_2O_3) [37]. After calcined in different atmospheres, both MIL-101 (Cr)-Air and MIL-101(Cr)-H_2 showed the coexistence of Cr^{6+} and crystalline Cr_2O_3 on the surface of the catalysts. After the treatment of 10 % O_2/Ar, the peak of Cr^{3+} on MIL-101(Cr)-Air-T didn't show significant change, with small increase in the relative peak intensity of Cr^{6+}. According to the literature, Cr^{6+} generated in an oxidative atmosphere was mainly derived from the transformation of coordinative unsaturated Cr^{3+} [39,40]. It implied that most of the Cr species had already form crystalline Cr_2O_3 during the calcination in the atmosphere of Air, and only a small part of Cr species existed in the form of coordinative unsaturated Cr^{3+}. For MIL-101(Cr)-H_2, the intensity of all the peaks due to crystalline Cr_2O_3 increased after the treatment of 10 %O_2/Ar. It seemed that although crystalline Cr_2O_3 was formed during the calcination in H_2/Ar, as shown in XRD results, some coordinative unsaturated Cr^{3+} species were still retained in the reduced atmosphere, producing more oxygen vacancies [30]. After the treatment of 10 %O_2/Ar, these coordinative unsaturated Cr^{3+} was oxidized to Cr^{6+} species. The phenomena of MIL-101(Cr)-Ar were different with the two catalysts above, only a weak peak assigned to Cr^{6+} was observed after the calcination in Ar, and no peaks corresponded to crystalline Cr_2O_3 were found. It seemed that there was little stable crystalline Cr_2O_3 formed during the calcination, which was also proved in the XRD results. Therefore, most of the Cr might still exist in the form of CrO_x clusters. After the treatment of 10 % O_2/Ar, crystalline Cr_2O_3 were formed, especially Cr^{6+}, proving the existence of large amount of coordinative unsaturated Cr^{3+}, which would transform to active Cr^{6+} [40].

3.1.4. XPS analysis

Further analysis of the surface elemental composition and elemental distribution of each catalyst after calcination and treatment of 10 %O_2/Ar was conducted by XPS. The results were shown in Fig. 2 and Table 2. The three peaks of C 1 s at 284.8, 286.3–286.4, and 288.4–288.6 eV were assigned to aromatic carbons C-C/C═C, C-O, and C═O, respectively [41,42]. Compared to Fig. 2(A), Fig. 2(D) showed a significant decrease in the peak corresponded to the aromatic carbons C-C/C═C on MIL-101(Cr)-H_2-T and MIL-101(Cr)-Ar-T. This indicated that the organic ligands in the catalysts were not completely removed during the calcination in the atmosphere of H_2/Ar and Ar, and more organic ligands were retained in MIL-101(Cr)-Ar.

The coordination form of Cr affected the chemical state distribution of Cr on the surface of the catalysts [31]. The Cr 2p spectra could be deconvoluted into three peaks, with binding energies at 575.3–575.9 eV, 576.4–576.9 eV, and 578.6–579.4 eV, assigning to the multisplit bands of Cr^{3+}, Cr^{3+}, and Cr^{6+} [14], respectively. It could be seen that Cr^{3+} was the main form of Cr on the surface of each catalyst, and the Cr^{6+} content was relatively low, both after calcination and treatment of 10 %O_2/Ar. The proportion of Cr^{6+} on the surface of all catalysts were almost equal around 22 % after the calcination, and the treatment of 10 %O_2/Ar caused a significant difference in Cr^{6+} proportion on each catalyst. Although the UV–vis spectra results showed an increase in the spectral response of Cr^{6+} on MIL-101(Cr)-Air-T after the treatment of 10 %O_2/Ar, the Cr^{6+} proportion detected by XPS only increased by 1.13 % (from 23.32 % to 24.45 % in Table 2). It proved again the lack of coordinative unsaturated Cr^{3+} on MIL-101(Cr)-Air, revealing the formation of stable crystalline Cr_2O_3 during the calcination in air. After the treatment of 10 %O_2/Ar, the Cr^{6+} proportion on the surface of MIL-101(Cr)-H_2-T increased 6.55 % (from 21.32 % to 27.87 % in Table 2), and that of MIL-101(Cr)-Ar-T increased 8.56 % (from 22.46 % to 31.02 % in Table 2). It was obvious that the amount of coordinative unsaturated Cr^{3+} on MIL-101(Cr)-Ar was the highest among the three catalysts. Cr^{6+} was reported with strong oxidative properties and was more active than Cr_2O_3 [14,38]. With the highest Cr^{6+} content, MIL-101(Cr)-Ar-T would be more favorable for the catalytic oxidation of CB.

The XPS O 1 s could be deconvoluted into three peaks. The peaks at 530.4, 531.9 and 533.8 eV were assigned to lattice oxygen (O_{latt}), surface adsorbed oxygen (O_{ads}) and hydroxyl groups (O_{OH}), respectively [43]. O_2 was activated to form O_{ads} and adsorbed on the oxygen vacancies [30], so the ratio of O_{ads}/O_{latt}, to some extent, could represent the content of oxygen vacancies[44]. The O_{ads}/O_{latt} ratio on MIL-101 (Cr)-Air was only 0.35, and it was 0.51 and 0.79 on MIL-101(Cr)-H_2 and MIL-101(Cr)-Ar, respectively. It seemed that the calcination in Air was not a good way to form oxygen vacancies. Part of the oxygen vacancies was formed accompanied with the coordinative unsaturated Cr^{3+} [45], therefore, the most coordinative unsaturated Cr^{3+} was retained in MIL-101(Cr)-Ar, then in MIL-101(Cr)-H_2. During the treatment of 10 %O_2/Ar, the coordinative unsaturated Cr^{3+} was oxidized to Cr^{6+} by O_2, resulting in the decrease of O_{ads}/O_{latt} ratio. MIL-101 (Cr)-Ar-T showed a considerable decrease, by 0.36, but still performed the highest ratio of O_{ads}/O_{latt} among the three catalysts. The oxidation of the coordinative unsaturated Cr^{3+} to Cr^{6+} led to the filling of some oxygen vacancies to form surface O_{latt} species [46]. Due to the abundant coordinative unsaturated Cr^{3+} on MIL-101(Cr)-Ar, it activated the most

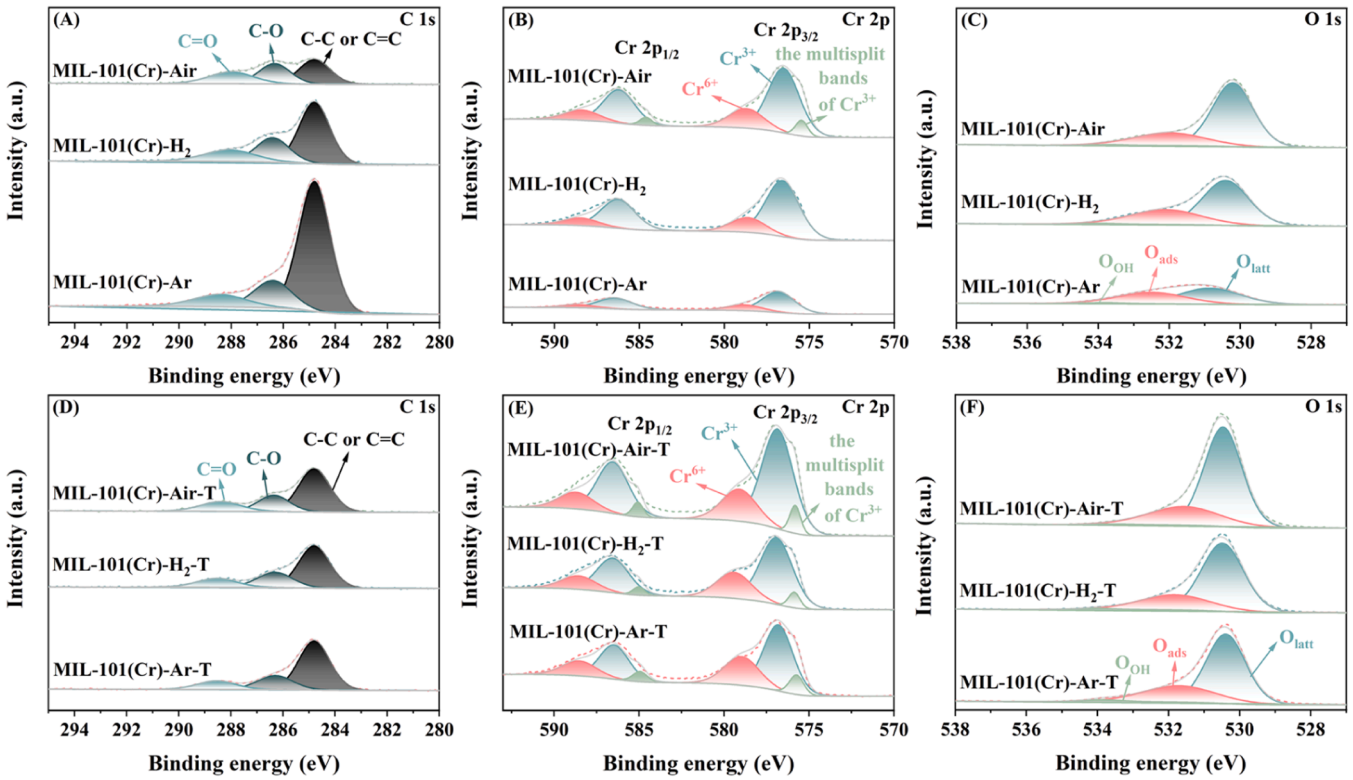

Fig. 2. XPS spectra of the catalysts after calcination (A) C 1 s, (B) Cr 2p, (C) O 1 s, and after treatment of 10 %O_2/Ar (D) C 1 s, (E) Cr 2p, (F) O 1 s.

Table 2
XPS results of the catalysts.

Catalysts	Cr (%)		O (%)			O_{ads}/O_{latt}
	Cr^{3+}	Cr^{6+}	O_{OH}	O_{ads}	O_{latt}	
MIL−101(Cr)-Air	76.68	23.32	0.46	26.03	73.51	0.35
MIL−101(Cr)-H_2	78.68	21.32	0.72	33.55	65.74	0.51
MIL−101(Cr)-Ar	77.54	22.46	1.28	43.52	55.21	0.79
MIL−101(Cr)-Air-T	75.55	24.45	0.50	24.26	75.24	0.32
MIL−101(Cr)-H_2-T	72.13	27.87	0.90	26.73	72.37	0.37
MIL−101(Cr)-Ar-T	68.98	31.02	1.71	29.76	68.52	0.43

O_2 during the treatment of 10 %O_2/Ar, thereby forming the highest amount of Cr^{6+}. Besides, the content of O_{OH} on MIL-101(Cr)-Ar-T was also the highest among the three catalysts, which was beneficial to the adsorption of CB [47].

3.1.5. *Tail gas composition during the calcination and treatment process*

To investigate the influence of the three calcination atmospheres on the catalysts, the tail gas composition during the calcination process was measured. As shown in Fig. S2, H_2O, CO, and CO_2 signals were observed in all three calcination atmospheres. Signals of C_6H_6 and C_7H_8 were additionally detected during the calcination in 10 %H_2/Ar, and signal of C_6H_6 was detected in the atmosphere of Ar. It indicated that the organic ligands in MIL-101(Cr) might be removed through different ways during the calcination process in the three atmospheres. The real-time variation of the composition in the tail gas was also measured and shown in Fig. 3. In the calcination atmosphere of Air (Fig. 3(A)), a large amount of CO, CO_2, and H_2O were generated with the consumption of O_2 in the temperature range of 240–350 °C. It revealed that the organic ligands were rapidly oxidized by O_2. Combined with the BET and XRD results, it was known that the micro-structure of the catalyst collapsed with the rapid removal of the organic ligands, and the CrO_x clusters were almost exposed and oxidized, forming stable crystalline Cr_2O_3. In the calcination atmospheres of 10 %H_2/Ar and Ar, the removal of organic ligands was much slower in the absence of O_2. As shown in Fig. 3(B) and (C), although the desorption of physically adsorbed water and ligand water molecules also appeared before 200 °C [48], the amount of CO and CO_2 produced over 200 °C was much lower than that in the calcination atmosphere of Air. Besides CO and CO_2, C_6H_6 was detected. It indicated that without O_2 in the calcination atmosphere, small part of the organic ligands could be oxidized by the O species on the catalyst to form CO and CO_2, and the benzene ring would then directly escape from organic ligands when the temperature went over 310 °C. The amount of the composition detected in the tail gas was much lower during the calcination in the atmosphere of 10 %H_2/Ar and Ar than in Air. Therefore, most of the organic ligands were not removed during the calcination in these two atmospheres. The unremoved organic ligands were carbonized and retained, which resulted in the detection of aromatic carbons C-C/C=C peaks in the XPS C 1 s spectra. The amounts of CO, CO_2, and C_6H_6 produced during the calcination process of MIL-101(Cr)-H_2 were higher than MIL-101(Cr)-Ar (Table S1), and C_7H_8 signal appeared along with the considerable consumption of H_2 in the temperature range of 350 to 500 °C, indicating that H_2 led to the hydrogenation of organic ligands, accelerating their removal. When the temperature reached 500 °C, a new peak of H_2O appeared with the consumption of a small amount of H_2. XRD and UV–vis spectra results showed crystalline Cr_2O_3 was formed in MIL-101(Cr)-H_2. Therefore, with the hydrogenation and removal of organic ligands, CrO_x clusters aggregated to form crystalline Cr_2O_3, the O in the crystals reacted with H_2, generating H_2O. It seemed that the organic ligands were removed in different ways in the three calcination atmospheres, and crystalline Cr_2O_3 was formed during the calcination in Air and H_2/Ar, while Cr still existing in the form of CrO_x clusters in Ar with more organic ligands retained.

The tail gas composition during the treatment of 10 %O_2/Ar was also measured, as shown in Fig. 3(D)-(F) and Table S2. CO_x was not detected in the tail gas during the treatment of MIL-101(Cr)-Air, indicating that all the organic ligands had completely removed in calcination process in Air. MIL-101(Cr)-H_2 and MIL-101(Cr)-Ar showed consumption of O_2 and generation of CO_x during the treatment process, and the amounts of

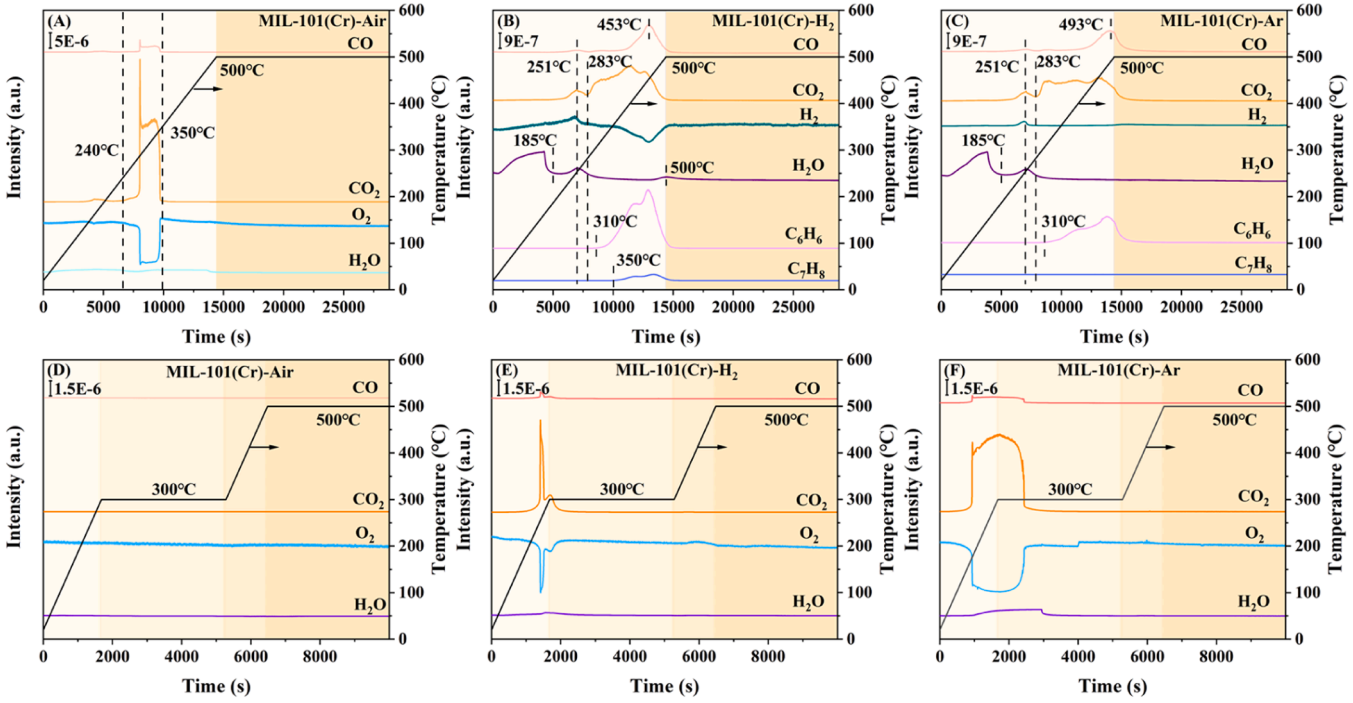

Fig. 3. MS signals for different compositions in the tail gas during the calcination in different atmospheres (A) Air, (B) 10 %H_2/Ar, (C) Ar, and the treatment of 10 % O_2/Ar (D) MIL-101(Cr)-Air, (E) MIL-101(Cr)-H_2, (F) MIL-101(Cr)-Ar.

CO and CO_2 in the tail gas of MIL-101(Cr)-Ar were 2.76 and 6.76 times higher than that of MIL-101(Cr)-H_2, respectively. It further demonstrated that more organic ligands were retained during the calcination in Ar than two other atmospheres. The unremoved organic ligands underwent carbonization, and worked as the carbon support to maintain the micro-structure and separate the CrO_x clusters from aggregating, resulting in the large number of coordinative unsaturated Cr^{3+} and oxygen vacancies on MIL-101(Cr)-Ar. During the treatment of 10 %O_2/Ar, the organic ligands were eventually removed through oxidation by O_2, and the coordinative unsaturated Cr^{3+} and oxygen vacancies combined with O_2 to form abundant Cr^{6+} and O_{ads} on the surface of MIL-101(Cr)-Ar-T, which was beneficial to the oxidation of CB. After the treatment of 10 %O_2/Ar, the temperature was further increased to 500 °C and maintained for 1 h. It could be found that no additional CO and CO_2 were generated during this process, which proved that the carbonized ligands had been completely removed during the treatment process. Besides, TGA results (Fig. S3) showed that the catalysts after treatment of 10 %O_2/Ar almost without mass loss at 300 °C, which further proved the removal of carbonization ligands and with good thermal stability.

3.2. Redox ability and oxygen mobility

The redox ability of the catalysts was investigated by H_2-TPR, as shown in Fig. 4. All catalysts showed four reduction peaks. The peak at 139 °C was assigned to the desorption of physically adsorbed water or the reduction of physical O_{ads}. The peak around 294 °C was assigned to the reduction of surface Cr^{6+} to Cr^{3+} [49]. The peak at 387 °C was assigned to the reduction of highly dispersed Cr^{3+} [38,50]. The last reduction peak around 479 °C was assigned to the reduction of crystalline Cr_2O_3 [38]. The H_2 consumption amount of the catalysts were calculated and shown in Table 3. Although MIL-101(Cr)-H_2-T and MIL-101(Cr)-Ar-T consumed similar amount of H_2 during H_2-TPR experiments, 2.20 and 2.21 times of MIL-101(Cr)-Air-T, respectively, there were great differences in the proportion of the reduction peaks. The Cr^{6+} reduction of MIL-101(Cr)-Ar-T accounted for 31.17 % of the total H_2 consumption, much higher than the 24.84 % of MIL-101(Cr)-H_2-T, indicating a high proportion of Cr^{6+} in MIL-101(Cr)-Ar-T. Compared

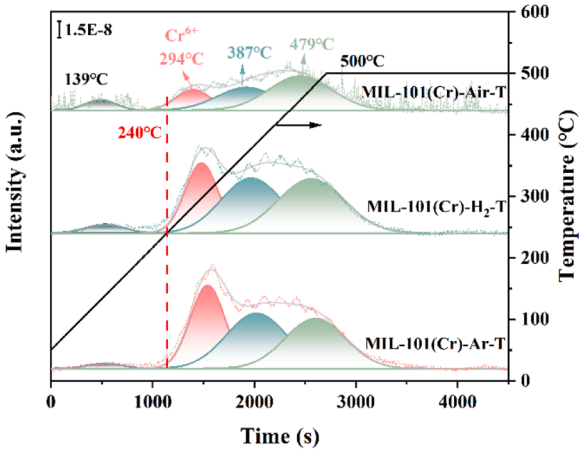

Fig. 4. H_2-TPR of the catalysts.

Table 3
Calculation results of H_2-TPR.

Catalysts	Total reduction peak area (a.u.)	Cr^{6+} (%)	Dispersed Cr^{3+} (%)	Crystalline Cr_2O_3 (%)
MIL−101 (Cr)-Air-T	2.10E−6	16.88	31.69	51.43
MIL−101 (Cr)-H_2-T	4.62E−6	24.84	35.98	39.18
MIL−101 (Cr)-Ar-T	4.65E−6	31.17	36.14	32.69

with the results of UV–vis spectra and XPS, the proportion of Cr^{6+} detected by H_2-TPR increased greatly on MIL-101(Cr)-Ar-T and decreased on other two catalysts. It suggested that Cr^{6+} was not only enriched on the surface of MIL-101(Cr)-Ar-T, a large part of Cr existed in the form of Cr^{6+} in its bulk phase. Among the three catalysts, the

proportion of crystalline Cr_2O_3 in the H_2 reduction was in the ordered as followed: MIL-101(Cr)-Ar-T < MIL-101(Cr)-H_2-T < MIL-101(Cr)-Air-T. The role of crystalline Cr_2O_3 was relatively minor compared to Cr^{6+} in the oxidation of Cl-VOCs below 300 °C [38], so the oxidation of Cl-VOCs at low temperatures was more related to the redox ability of Cr^{6+}. Obviously, the high content of Cr^{6+} on MIL-101(Cr)-Ar-T was more conducive to the low-temperature oxidation of CB.

The redox cycle between Cr^{6+} and Cr^{3+} in the reaction was very important for the oxidation of CB [14,51], and the Cycled H_2-TPR experiment was carried out to investigate the redox behavior of Cr species. The H_2-TPR results in Fig. 4 showed that the reduction peaks of Cr^{6+} and dispersed Cr^{3+} overlapped in a broad temperature range. To avoid the influence of dispersed Cr^{3+} on the reduction peak of Cr^{6+}, the Cycled H_2-TPR experiment was carried out up to 240 °C, and Cr^{6+} could be reduced without the reduction of dispersed Cr^{3+}. Therefore, H_2 consumption was mainly from the reduction process of Cr^{6+}. In Cycled H_2-TPR-1 experiment, the catalysts were re-oxidized by O_2 after 5 cycles of the reduction, and then reduced again, to investigate the regeneration of Cr^{6+} by gas phase O_2. As shown in Fig. 5(A) and Table 4, the H_2 consumption of Cr^{6+} in all catalysts decreased a lot after the first cycle. After 5 cycles, the H_2 consumption of Cr^{6+} reduction in MIL-101 (Cr)-H_2-T and MIL-101(Cr)-Ar-T was 34.11 % and 37.24 % of the first cycle, respectively. After 5 cycles of reduction, 10 %O_2/Ar was introduced to the catalysts to regenerate Cr^{6+}, and the reduction was carried out again. Each catalyst showed an apparent peak due to the reduction of Cr^{6+}, indicating that part of the reduced Cr species could be re-oxidized to Cr^{6+} by O_2. The H_2 consumption of Cr^{6+} reduction after the regeneration was calculated and compared with that of the first reduction. It was found that MIL-101(Cr)-Ar-T could regenerate 97.66 % of Cr^{6+}, and it was 91.55 % and 82.58 % for MIL-101(Cr)-H_2-T and MIL-101(Cr)-Air-T, respectively. MIL-101(Cr)-Ar-T showed a higher ability for O utilization and regeneration of Cr^{6+}.

It was reported that O_{latt} in the catalyst could migrate to the surface through oxygen vacancies to replenish the consumption of the oxygen around high-valence metal in the reaction [52], and Cycled H_2-TPR-1 experiment revealed the different H_2 consumption ratio of the fifth cycle to the first cycle on each catalyst. Cycled-H_2-TPR-2 experiment was carried out to investigate the migrations of the O_{latt} in each catalyst. After 3 cycles of reduction to 240 °C, the temperature was raised to 500 °C in the fourth cycle, and the H_2 consumption was compared with the results of H_2-TPR experiment in Fig. 4, as shown in Fig. 5(B). The peak due to Cr^{6+} reduction showed an apparent decrease in all catalysts, indicating that most of Cr^{6+} had been reduced during the 3 cycles of reduction. It was worth noting that the reduction peaks assigned to highly dispersed Cr^{3+} and crystalline Cr_2O_3 also decreased in MIL-101 (Cr)-H_2-T and MIL-101(Cr)-Ar-T, while MIL-101(Cr)-Air-T showing little

Table 4
H_2 Consumption of catalysts.

Catalysts	Cycled H_2-TPR-1	Cycled H_2-TPR-2	
	Cr^{6+} recovery (%)[a]	Dispersed Cr^{3+} (%)[b]	Crystalline Cr_2O_3 (%)[c]
MIL−101(Cr)-Air-T	82.58	8.08	9.54
MIL−101(Cr)-H_2-T	91.55	13.77	15.47
MIL−101(Cr)-Ar-T	97.66	20.83	22.37

[a] The results were calculated by $A_{recovery}/A_1^{st}{}_{cycle}$ in Fig. 5(A).
[b] The results were calculated by the decreased ratio of dark cyan peak compared with the peak of light cyan in Fig. 5(B).
[c] The results were calculated by the decreased ratio of dark green peak compared with the peak of light green in Fig. 5(B).

variation. Since highly dispersed Cr^{3+} and crystalline Cr_2O_3 could not be reduced at 240 °C, the decrease in the intensity of these two reduction peaks should be attributed to the migration of O_{latt} through oxygen vacancies during the 3 reduction cycles at 240 °C, which could replenish the oxygen consumed around Cr^{6+}, and made Cr^{6+} maintain at the high valence. Among the three catalysts, MIL-101(Cr)-Ar-T showed the most considerable decrease in the reduction peak intensity of highly dispersed Cr^{3+} and crystalline Cr_2O_3, reduced by 20.83 % and 22.37 % respectively (Table 4), indicating that it was rich in oxygen vacancies, and more O_{latt} could migrate to replenish the oxygen around Cr^{6+}, which resulted in the higher H_2 consumption by Cr^{6+} in the fifth cycle in Cycled H_2-TPR-1 experiment.

The properties of oxygen in the three catalysts were further investigated by O_2-TPD, as shown in Fig. 6 and Table 5. The O_2-TPD desorption peaks in the graph were mainly divided into three regions. Peaks below 300 °C were assigned to the desorption of surface physically O_{ads} (α) [53], and all three catalysts showed low amount of α-O. The peaks in the range of 300–600 °C were assigned to the desorption of chemical O_{ads} and surface O_{latt} (β) [47]. Peaks above 600 °C were assigned to the desorption of bulk O_{latt} (γ) [47,54]. The β-O on the surface was considered as the active oxygen center, since it was more easily involved in reactions, thereby promoting the deep oxidation of CB [47]. MIL-101 (Cr)-Air-T had the smallest amount of O_2 desorption and a relatively low β-O content. Its main desorption peak was the bulk O_{latt}, accounting for 62.18 % of the total O_2 desorption, indicating that oxygen species on MIL-101(Cr)-Air-T mainly existed in the form of bulk O_{latt}, therefore, it showed low migration ability in Fig. 5(B). Compared to MIL-101 (Cr)-Air-T, the O_2 desorption content of the other two catalysts was much higher. Especially the β-O content on MIL-101(Cr)-Ar-T, it increased to 11.32 times of that on MIL-101(Cr)-Air-T, both O_{ads} and

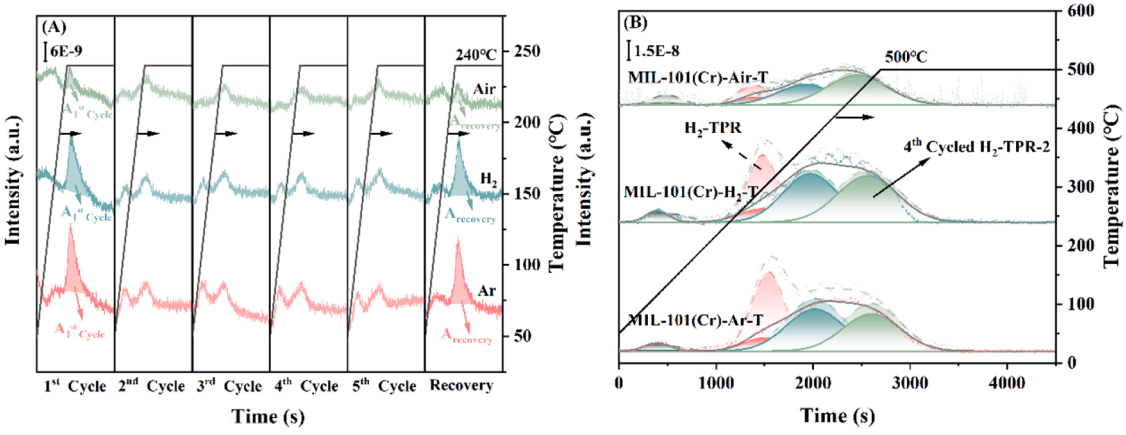

Fig. 5. (A)The Cycled H_2-TPR-1 of MIL-101(Cr)-Air-T (green), MIL-101(Cr)-H_2-T (cyan) and MIL-101(Cr)-Ar-T (red), (B) The variation of 4th Cycled H_2-TPR-2 (solid line) compared to normal H_2-TPR (dashed line).

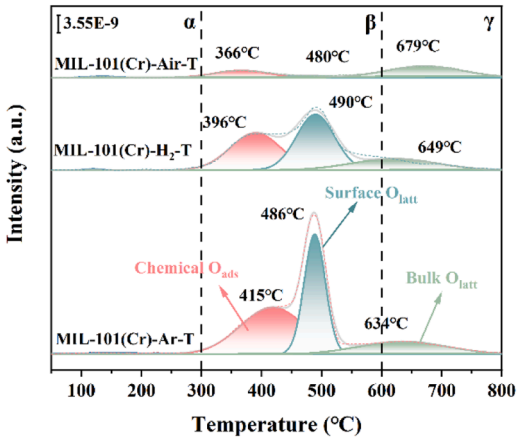

Fig. 6. O_2-TPD of the catalysts.

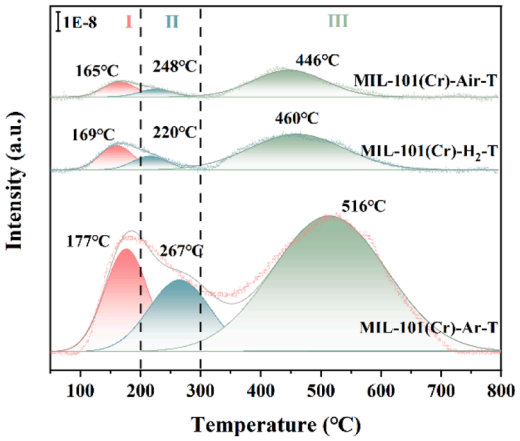

Fig. 7. NH_3-TPD of the catalysts.

Table 5
Calculation results of O_2-TPD.

Catalysts	α (%)	β (%)		γ (%)	Total desorbed oxygen (a.u.)
		Chemical O_{ads}	Surface O_{latt}		
MIL−101 (Cr)-Air-T	3.05	28.16	6.61	62.18	2.88E−8
MIL−101 (Cr)-H_2-T	0.3	37.81	42.85	19.03	1.01E−7
MIL−101 (Cr)-Ar-T	1.99	44.39	37.17	16.44	1.39E−7

surface O_{latt} increased greatly. It was reported that most of the surface O_{ads} was linked to the metal with high valence due to the presence of the oxygen vacancies [55]. Therefore, the high amount of O_{ads} on MIL-101 (Cr)-Ar-T (Table 5) was caused by the abundant Cr^{6+}, as well as the oxygen migration through oxygen vacancies, as proved by in XPS and Cycled H_2-TPR results. Furthermore, the proportion of bulk O_{latt} decreased when the catalysts were calcined in the atmosphere of H_2/Ar and Ar, and the desorption temperature also shifted to lower temperature. Different calcination atmosphere played important roles in the redox ability, more β-O as the active oxygen center and oxygen vacancies were formed on MIL-101(Cr)-Ar-T, leading to its higher Cr^{6+} regeneration ability and oxygen migration ability. The content of oxygen vacancies was further characterized by EPR, as shown in Fig. S4, the catalysts exhibited different intensity of EPR signals at g = 2.003, which could be attributed to the existence of oxygen vacancies [53]. It could be found that MIL-101(Cr)-Ar-T exhibited the strongest EPR signal intensity, indicating that there were more oxygen vacancies on MIL-101 (Cr)-Ar-T, which was consistent with the above results.

3.3. Surface acidity and activation of CB

In addition to the active oxygen, the surface acidity of the catalyst also affected the catalytic activity through the adsorption and oxidation of CB. NH_3-TPD was conducted to analyze the surface acidity distribution of the catalysts. As shown in Fig. 7 and Table S3, the desorption peaks of NH_3-TPD could be divided into three regions. Region I (<200 °C) was assigned to the desorption of adsorbed ammonia on Brønsted acid sites. Region II (200–300 °C) was assigned to the desorption of adsorbed ammonia on mild Lewis acid sites. Region III (>300 °C) was assigned to the desorption of adsorbed ammonia on strong Lewis acid sites [56,57]. Brønsted acid sites were derived from hydroxyl groups on the catalyst surface [47], which were formed from the surface O_{ads} and water, and would be promoted by the oxygen vacancies [58]. In Fig. 7, the amount of Brønsted acid sites on MIL-101 (Cr)-Ar-T was 8.75 and 5.46 times of that on MIL-101(Cr)-Air-T and MIL-101(Cr)-H_2-T, respectively. It might be due to the high amount of oxygen vacancies and O_{ads} on MIL-101(Cr)-Ar-T, as proved by XPS and O_2-TPD results. Lewis acid sites were derived from Cr^{3+}/Cr^{6+}. Cr^{6+}, as a highly electron-deficient strong Lewis acid site, had strong oxidative properties [14,59]. According to UV–vis spectra, XPS, and H_2-TPR results, MIL-101(Cr)-Ar had abundant coordinative unsaturated Cr^{3+} after the calcination in the atmosphere of Ar, and then formed a large amount of Cr^{6+} after the treatment of 10 %O_2/Ar. Therefore, MIL-101(Cr)-Ar-T showed the highest content of strong Lewis acid sites, 7.96 and 4.58 times than that of MIL-101(Cr)-Air-T and MIL-101(Cr)-H_2-T, respectively. Brønsted acid sites were considered with important effect for adsorption/activation of CB and the desorption of inorganic Cl, and strong Lewis acid sites could promote the deep oxidation of intermediates [47,60]. Therefore, the high acid content gave MIL-101 (Cr)-Ar-T an advantage in the oxidation of CB.

The adsorption and activation of CB on the catalysts was studied by CB-TPD, and the results were shown in Fig. 8 and Table S4. All three catalysts showed CB desorption peaks in the range of 120–130 °C. Among them, the CB desorption peak on MIL-101(Cr)-Ar-T was the largest, with an area 31.59 and 5.81 times of that on MIL-101(Cr)-Air-T and MIL-101(Cr)-H_2-T, respectively. To eliminate the influence of specific surface area on the adsorption of CB, the CB desorption peaks were normalized through dividing them by the specific surface area of each catalyst, as shown in Fig. S5. After normalization, the order of the CB desorption peak intensity per unit specific surface area remained unchanged. The CB desorption per unit specific surface area on MIL-101 (Cr)-Ar-T remained 4.92 and 2.23 times of that on MIL-101(Cr)-Air-T and MIL-101(Cr)-H_2-T, respectively. This indicated that the adsorption of CB was not determined by the specific surface area of the catalysts. The relationship between the CB adsorption and the Brønsted acid sites was analyzed (Fig. S6), and it was found that they had good linear relationship on all three catalysts (R^2 =0.9958), indicating that the adsorption of CB was mainly determined by the amount of Brønsted acid sites. Although O_2 was in absence in the CB-TPD experiment, part of the CB was still oxidized and Cl species were desorbed during the desorption process of CB. Since Cl_2 was mainly generated through the Deacon reaction at temperatures above 250 °C [61], only the HCl signal was observed in the spectrum during the desorption of CB below 240 °C. Although the signal value was low, it was still evident that the amount of HCl produced on MIL-101(Cr)-Ar-T was higher than the other two catalysts. This might be due to the most Brønsted acid sites on its surface, promoting the dechlorination of CB. Additionally, CO and CO_2 signals were also observed during the desorption process of CB, indicating that some adsorbed CB was oxidized. With the highest amount of Cr^{6+}, MIL-101(Cr)-Ar-T exhibited the most Lewis acid sites and O_{ads}, therefore, more CB was oxidized, and the CO_x produced was 3.05 and 1.09

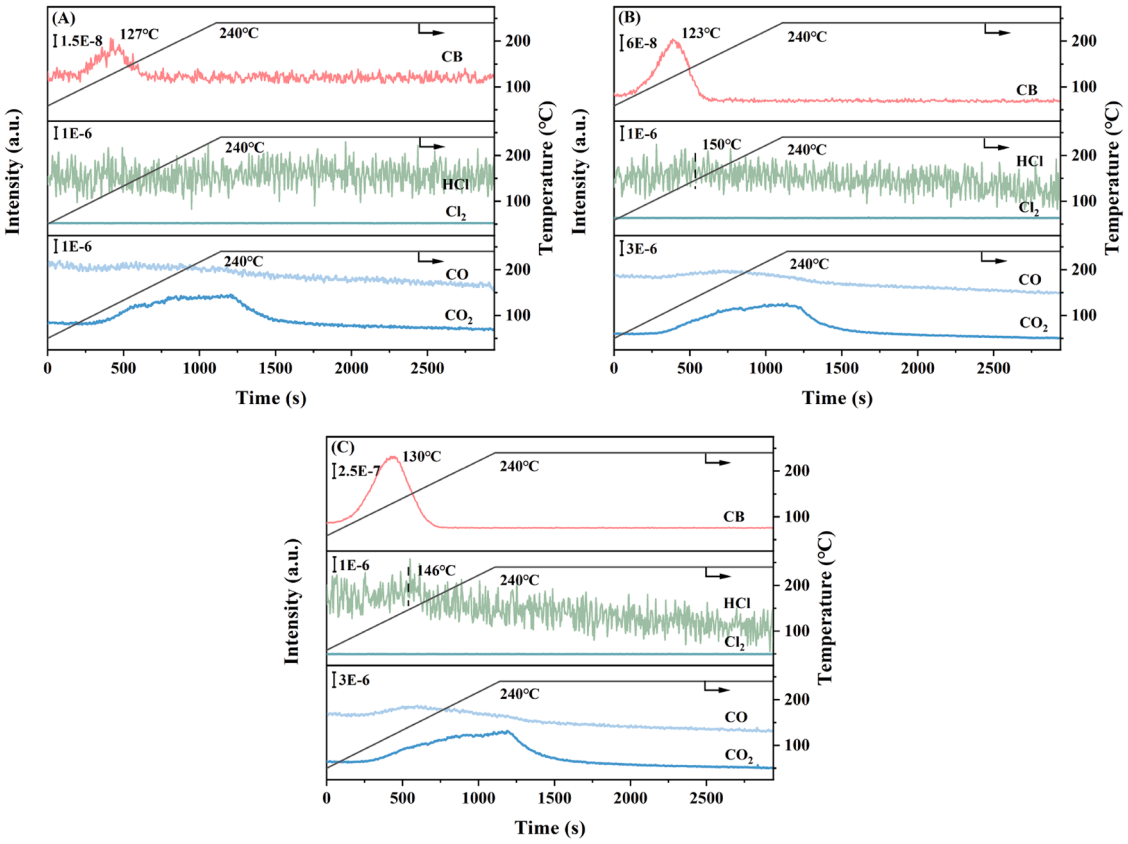

Fig. 8. CB-TPD of the catalysts (A) MIL-101(Cr)-Air-T, (B) MIL-101(Cr)-H_2-T, (C) MIL-101(Cr)-Ar-T.

times of that on MIL-101(Cr)-Air-T and MIL-101(Cr)-H_2-T, respectively.

3.4. Catalyst activity

The catalytic activity of the three catalysts for CB oxidation was tested, with CrO_x-P-T prepared by precipitation as a reference, as shown in Fig. 9. The CB conversion of all catalysts increased with the temperature (Fig. 9(A)). The catalytic activity of each catalyst was evaluated by the temperature required to achieve 90 % CB conversion (T90). The T90 values for the four catalysts were 233 °C on MIL-101(Cr)-Ar-T, 253 °C on MIL-101(Cr)-H_2-T, 273 °C on MIL-101(Cr)-Air-T, and 280 °C on CrO_x-P-T. This indicated that the catalyst prepared from MIL-101(Cr) as precursor was more active for the oxidation of CB than that by traditional method. More importantly, the different calcination atmospheres had further effect on the catalytic activity. The calcination atmosphere of Ar was obviously more favorable to obtain the high catalytic activity. The CO_x selectivity was shown in Fig. 9(B). All catalysts were able to achieve over 90 % CO_x selectivity in the high temperature range of 260–300 °C. However, in the lower temperature range of 200–240 °C, only MIL-101(Cr)-Ar-T maintained CO_x selectivity over 90 %. On MIL-101(Cr)-Ar-T, more CB could be adsorbed and converted, and the intermediates during the CB oxidation were easily to be further oxidized to CO_x at lower temperature.

Based on the differences in the CB oxidation at 240 °C, this temperature was selected to test the selectivity of Cl after the conversion of CB, the results were shown in Table S5. The MIL-101(Cr)-Ar-T exhibited the highest HCl selectivity of 97.61 %, and the rest Cl was converted to Cl_2. The used catalysts were also detected by XPS, as shown in Fig. S7, Table S6 and Table S7. the atomic concentration of Cl was only 0.37 % on MIL-101(Cr)-Ar-T. With almost 100 % of Cl coming out to gas phase, little Cl would react with the metal on the surface of the catalysts.

The stability experiment of MIL-101(Cr)-Ar-T at 240 °C in Fig. 9(C) showed that it could maintain nearly 100 % CB conversion in 5-day oxidation reaction. Therefore, MIL-101(Cr)-Ar-T exhibited the highest catalytic activity for CB oxidation. Since there might be SO_2 in the waste incineration flue gas, the experiment of resistance to sulfur poisoning was also carried out. Fig. 9(D) exhibited the variation of CB conversion and CO_x selectivity on MIL-101(Cr)-Ar-T after the addition of SO_2. The conversion of CB was stable, and only the CO_2 selectivity was reduced by about 8 %, indicating that MIL-101(Cr)-Ar-T with high resistance to sulfur poisoning. Table S8 showed the comparison of different MOF-derived catalysts and metal oxide catalysts reported in recent years with the MIL-101(Cr)-Ar-T in CB catalytic oxidation, from which it could be observed that MIL-101(Cr)-Ar-T has significant advantages on CB catalytic oxidation at low oxygen concentration and low temperature.

3.5. In situ DRIFTs measurements

In order to reveal the reaction pathway of CB oxidation on the surfaces of different catalysts, in situ DRIFTs experiments were carried out to observe the variation of the intermediates during the oxidation of CB at 240 °C, as shown in Fig. 10(A)-(C). Similar vibrational peaks appeared around 1660, 1621, 1590, 1552, 1540, 1514, 1426, 1411, 1375, 1356, 1311, and 1280 cm^{-1}, indicating that the intermediates formed on during the reaction were similar on the three catalysts. The assignments of the peaks were summarized in Table 6. According to the literature, the bond energy of the C-Cl bond was 339 kJ/mol, much lower than C-H bond at 414 kJ/mol, so the first step of the catalytic oxidation of CB was the breaking of the C-Cl bond [62]. The production after C-Cl bond breaking was related to Brønsted acid sites, and it would form phenol on the surface rich in Brønsted acid sites, while forming benzene on the surface lacked of Brønsted acid sites [61]. NH_3-TPD results showed that the amount of Brønsted acid sites on MIL-101(Cr)-Ar-T was much higher than that on other two catalysts. In Fig. 10, the intensity of peak at 1280 cm^{-1} due to phenol was the highest on MIL-101 (Cr)-Ar-T of the three catalysts, and MIL-101(Cr)-Air-T showed the

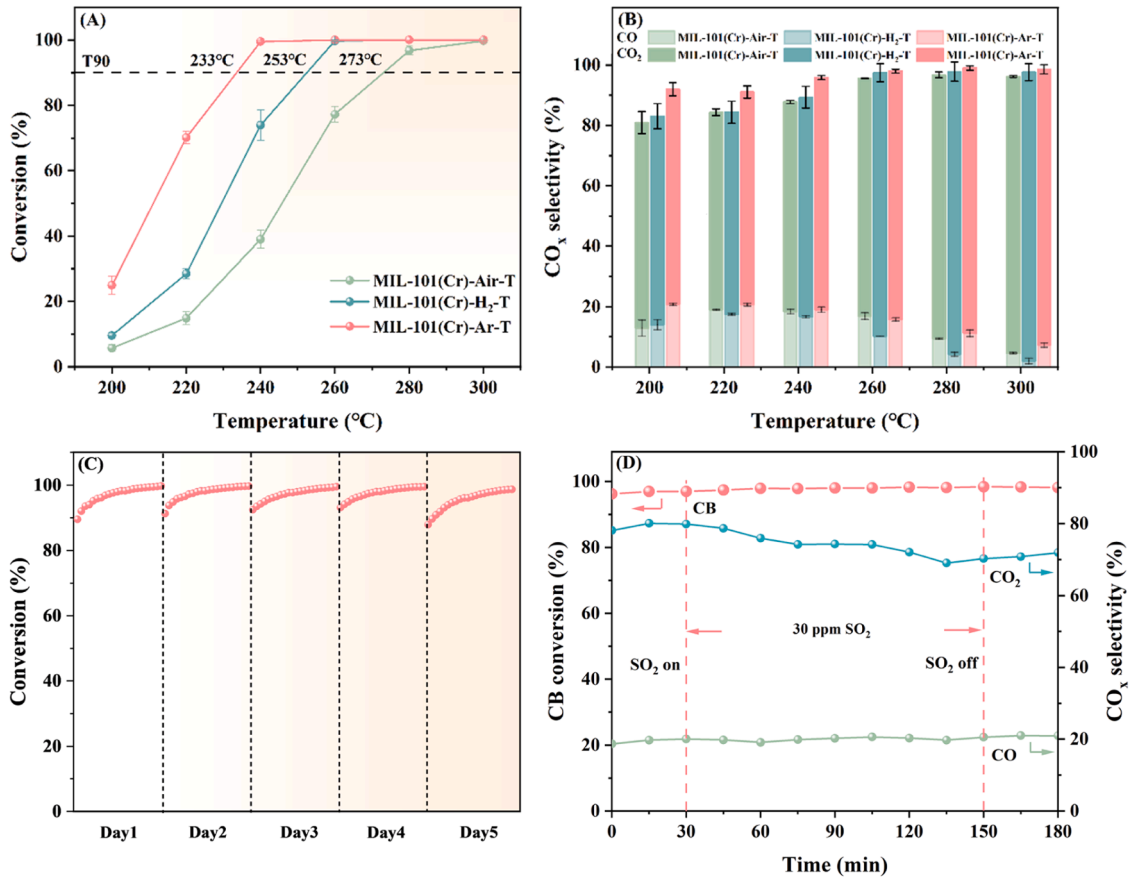

Fig. 9. The catalytic activity of the catalysts. (A) CB conversion, (B) CO_x selectivity, (C) the stability of MIL-101(Cr)-Ar-T at 240 °C, (D) the resistance to sulfur poisoning of MIL-101(Cr)-Ar-T at 240 °C (Reaction conditions: 100 ppm CB, 30 ppm SO_2 when used, 10 %O_2 and N_2 balance; WHSV = 40000 mL/(g·h); catalyst amount: 75 mg).

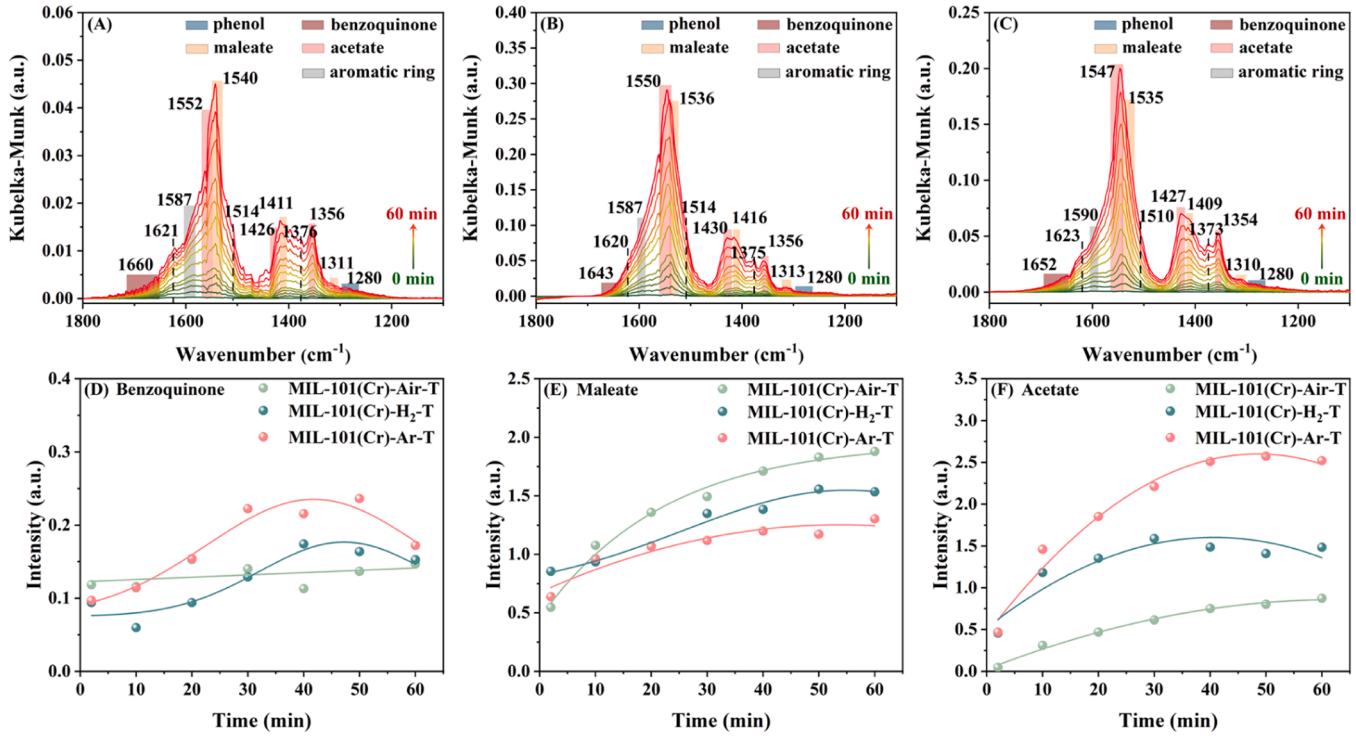

Fig. 10. In situ DRIFTs spectra of (A) MIL-101(Cr)-Air-T, (B) MIL-101(Cr)-H_2-T, (C) MIL-101(Cr)-Ar-T in CB and 10 %O_2 collected at 240 °C (balanced by Ar), and the evolution of surface (D) benzoquinone, (E) maleate, (F) acetate over different catalysts.

Table 6
Observed DRIFT vibration frequencies (cm^{-1}) of intermediate species in CB oxidation.

Wavenumber (cm^{-1})	Assignment	Ref.
1646 −1660	benzoquinone (C═O stretching vibration)	[65]
~ 1623	o-benzenediol	[66]
1590	aromatic ring (C═C stretching vibration)	[67, 68]
1552, 1547	acetate (COO^- asymmetric stretching vibration)	[68]
1540 −1536, 1416 −1409, 1313 −1310	maleate	[68, 69]
1514, 1510	adsorbed benzene	[61, 70]
1430 −1426	acetate (COO^- symmetric stretching vibration)	[69]
1356 −1354	acetate (CH_3 stretching vibration)	[1]
1376 −1373	formate (COO^- stretching vibration)	[71]
1280	phenol (C-O stretching vibration)	[68]

strongest the peak around 1514 cm^{-1} due to adsorbed benzene. The amount of phenol did not increase with time, since phenol was easily transformed into o-benzoquinone and p-benzoquinone due to the property that the oxygen-containing group was generally regarded as an electron donating group and an ortho-para position director [63,64]. Therefore, a vibration peak near 1623 cm^{-1} assigned to o-benzenediol and C═O stretching vibration peaks around 1660–1646 cm^{-1} due to benzoquinone species were observed. In addition, vibration peaks of the intermediates after ring-opening were also found, such as the peaks at 1540–1536, 1416–1409, 1313–1310 cm^{-1} assigned to the vibration of maleate, peaks at 1552–1547 cm^{-1} assigned to the COO^- asymmetric stretching vibration of acetate, peaks at 1430–1426 cm^{-1} assigned to the COO^- symmetric stretching vibration of acetate, peaks at 1356–1354 cm^{-1} assigned to the CH_3 stretching vibration of acetate, and peaks at 1376–1373 cm^{-1} assigned to the COO^- stretching vibration of formate. They were all intermediates during the deep oxidation after ring-opening by the surface O_{ads} on strong Lewis acid sites [47], resulting in maleate, and then further oxidized to acetate and formate, and eventually to CO, CO_2 and H_2O. It could be observed from Fig. 10 that the accumulation of various intermediates on the three catalysts was different, indicating that there were differences in the processes of CB oxidation. Therefore, the peak fitting was carried out for six peaks at 1660, 1621, 1590, 1552, 1540 and 1514 cm^{-1} (Fig. S10(A)-(C)), to investigate the variation of the main intermediates, such as benzoquinone, maleate, and acetate, and then to reveal key steps for CB oxidation on different catalysts.

The adsorption of CB was the first step of CB oxidation, therefore, the peak intensity of the aromatic ring C═C bond at 1590 cm^{-1} was selected as a reference point for assessing the conversion and/or accumulation of other intermediates during the oxidation process. The variation of intermediates with time was shown in Fig. 10(D)-(F). Fig. 10(D) showed the variation of benzoquinone. The amount of benzoquinone on MIL-101(Cr)-Air-T was relatively stable, showing an extremely slow increase from 0 to 60 min. Benzoquinone was mostly derived from the oxidation of phenol [1]. However, phenol was difficult to be formed on MIL-101(Cr)-Air-T due to the lack of Brønsted acid sites, resulting in a relatively low content of benzoquinone. The stable content of benzoquinone indicated that it could not be oxidized rapidly, even with low content. Therefore, the oxidation ability of MIL-101(Cr)-Air-T was weak. On the surface of MIL-101(Cr)-H_2-T and MIL-101(Cr)-Ar-T, the content of benzoquinone increased from 0 to 40 min and then gradually decreased in the following 20 min. It indicated that CB could be converted to phenol through the abundant Brønsted acid sites on the two catalysts, especially on MIL-101(Cr)-Ar-T, and then further oxidized to benzoquinone. Benzoquinone would not accumulate on the two catalysts during the reaction. After 40 min, the large number of O_{ads} linked to Cr^{6+} on the surface of MIL-101(Cr)-Ar-T accelerated the oxidation of benzoquinone, resulting in a higher rate of decrease in benzoquinone compared to MIL-101(Cr)-H_2-T. Fig. 10(E) and (F) showed the variation of maleate and acetate after the ring-opening of benzoquinone. It was reported that maleate was an important intermediates in the reaction process and could stably exist on the catalyst surface [72]. The maleate content on MIL-101(Cr)-Air-T was the lowest at 2 min, and then increased rapidly, exceeding that on MIL-101(Cr)-H_2-T and MIL-101(Cr)-Ar-T within just 10 min. Due to the limited content of benzoquinone, the increase of maleate content on MIL-101(Cr)-Air-T should not be resulted by its large production, and acetate, as the subsequent oxidation product of maleate, remained at a low level throughout the reaction process. This indicated that the oxidation of maleate was inhibited due to the limited oxidation ability of MIL-101(Cr)-Air-T, leading to the rapid accumulation of maleate on the surface. The content of maleate on MIL-101(Cr)-Ar-T was at a low level during the reaction process. However, the content of acetate on MIL-101(Cr)-Ar-T increased rapidly within the first 40 min and then became stable, much higher than other two catalysts. The low content of maleate was caused by the rapid oxidation to acetate, so it could not accumulate on the surface of MIL-101(Cr)-Ar-T. In summary, during the oxidation of CB on MIL-101(Cr)-Ar-T, the large number of Brønsted acid sites promoted the conversion of CB to phenol, which was rapidly oxidized by the high amount of O_{ads} on the strong Lewis acid sites, forming maleate, acetate, finally producing CO_x and H_2O. Therefore, it showed the highest CB conversion and CO_x selectivity at low temperature.

3.6. DFT calculations

It has been proved by in situ DRIFTs that when CB was converted to benzoquinone species, they were much easier to be oxidized on MIL-101(Cr)-Ar-T, which was rich in oxygen vacancy and with active migration of lattice oxygen. Besides the oxidation from benzoquinone, the process of the CB adsorption and conversion was also investigated by DFT calculations, as shown in Fig. 11. MIL-101(Cr)-Air-T and MIL-101(Cr)-Ar-T was set as two models. Both the presence and amount of oxygen vacancies could influence the length of Cr-O bond. In MIL-101(Cr)-Air-T, the length of Cr-O bond near the oxygen vacancies was 1.976 Å, and that away from the oxygen vacancies was only 1.935 Å. As for MIL-101(Cr)-Ar-T, the length of Cr-O bond became 2.124 Å and 2.028 Å, respectively. The high amount of Cr^{6+} near the oxygen vacancies would elongate the Cr-O bond through Jahn-Teller effect, resulting in more active lattice oxygen participating in the reaction [73]. During the adsorption of CB, the adsorption energies of CB on MIL-101(Cr)-Air-T and MIL-101(Cr)-Ar-T surfaces were −0.86 eV and −3.91 eV, respectively, indicating that MIL-101(Cr)-Ar-T could adsorb CB easily. After the adsorption, the length of C-Cl bond in MIL-101(Cr)-Ar-T was longer, with 1.814 Å, promoting the dissociation of C-Cl. Meanwhile, the Cr-O bond near and away from oxygen vacancies was further elongate to 2.139 Å and 2.093 Å, which further oxidized the reaction intermediates, and then resulting in the quick transformation of benzoquinone, maleate and acetate in Fig. 10.

The variation in different calcination atmospheres, and its role on the activity of the catalysts was revealed by the experiments and shown in Fig. 12. In the calcination atmosphere of Air or 10 % H_2/Ar, the organic ligands in MIL-101(Cr) were completely or mostly removed, and the CrO_x metal clusters aggregated and were oxidized to form stable crystalline Cr_2O_3. In contrast, large amounts of organic ligands were carbonized and retained in the atmosphere of Ar. It made the catalyst remain part of the micropore structure and high specific surface area, thus promoting the dispersion and exposure of Cr. Therefore, the CrO_x clusters were preserved by the separation of carbonized ligands, and there were abundant coordinative unsaturated Cr^{3+} and oxygen vacancies on the surface of after calcination. During the treatment of 10 % O_2/Ar, coordinative unsaturated Cr^{3+} species was oxidized to Cr^{6+} with the transformation of the CrO_x clusters to crystalline Cr_2O_3. With the

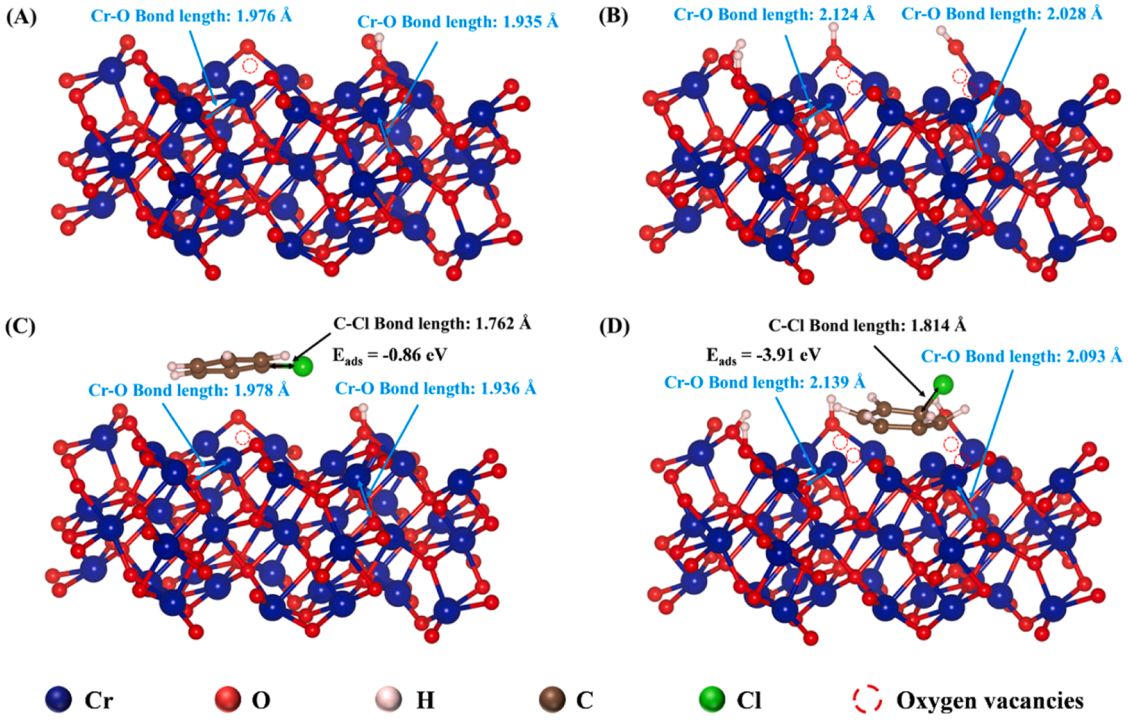

Fig. 11. Calculated lattice structures of (A) MIL-101(Cr)-Air-T and (B) MIL-101(Cr)-Ar-T; surface models of CB adsorption on (C) MIL-101(Cr)-Air-T and (D) MIL-101 (Cr)-Ar-T.

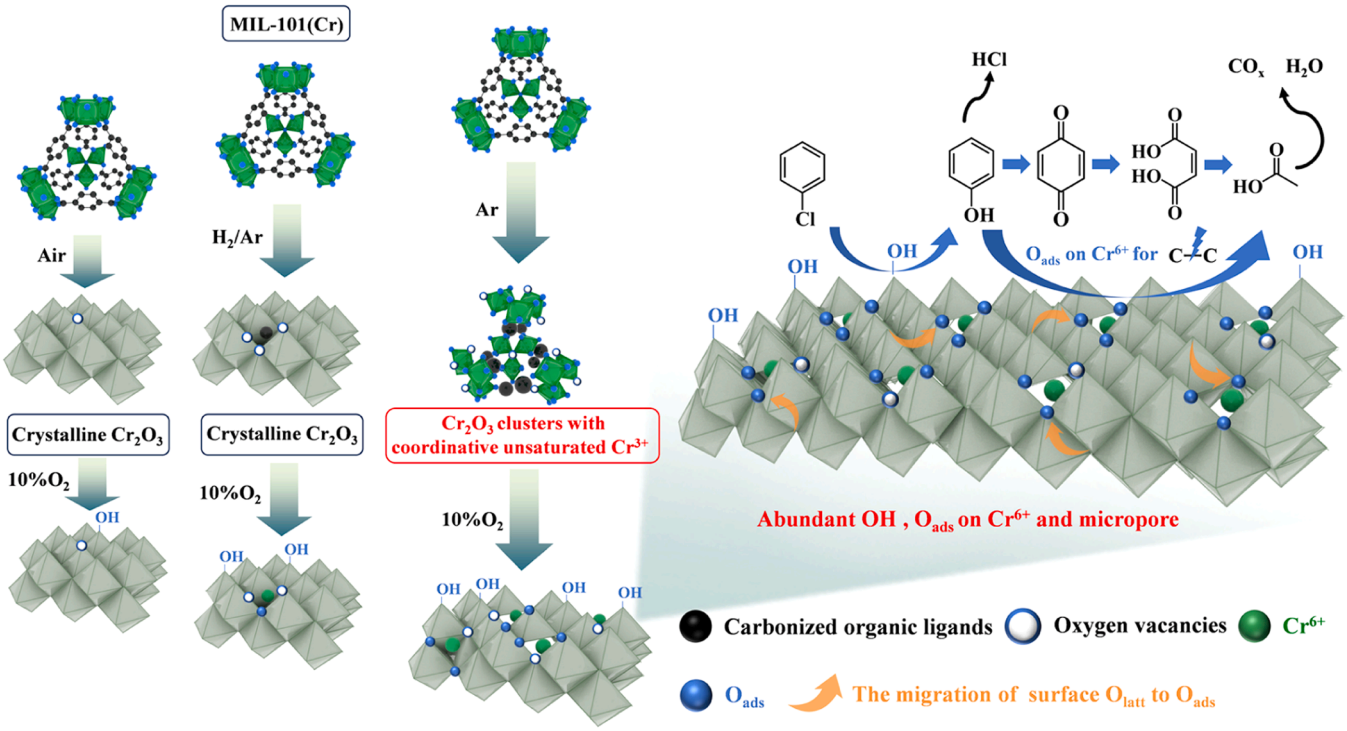

Fig. 12. The variation of MIL-101(Cr) in different calcination atmospheres and the pathway of CB oxidation.

effect of oxygen vacancies, large amounts of OH and O_{ads} on Cr^{6+} were produced, forming abundant Brønsted acid sites and strong Lewis acid sites, respectively. Therefore, the adsorption and activation of CB was promoted by OH, leading to the formation of phenol and production of HCl. During the further oxidation of intermediates, the O_{ads} on Cr^{6+} as strong Lewis acid sites enhanced the cleavage of C-C bonds, and the consumption of O_{ads} could be rapidly replenished by the migration of surface O_{latt}. With the effects above, CB could be converted and the intermediates could be deeply oxidized to CO_x at lower temperature.

4. Conclusion

This study investigated the influence of different calcination atmospheres (Air, 10 %H_2/Ar, Ar) on the physicochemical properties of MIL-101(Cr) catalysts, and the performance for the oxidation of CB. Among three calcination atmospheres, only Ar atmosphere achieved the stepwise removal of organic ligands. During the calcination, part of organic ligands was were carbonized and remained. The carbonized organic ligands prevented the aggregation of CrO_x clusters, maintaining the physical structure, as well as large amounts of coordinative unsaturated Cr^{3+} and oxygen vacancies. This led to the high content of OH from Brønsted acid sites, which enhanced the adsorption/activation of CB, and abundant O_{ads} on Cr^{6+} as the strong Lewis acid sites that further oxidized the intermediates. The migration of surface O_{latt} could replenish the O_{ads} consumed around Cr^{6+} during the reaction. This resulted in 100 % CB conversion at 240 °C, and the selectivity of 97.6 % and 95 % to HCl and CO_x selectivity, respectively.

Environmental Implication

Chlorobenzene, as one of the typical precursors of polychlorinated biphenyls and furans, has enormous damage to health of human and eco-environment. Therefore, chlorobenzene is widely known as a toxic "hazardous material", which would give rise to atmospheric ozone, photochemical smog, cancerization and distortion of organism. We used MIL-101(Cr)-derived CrO_x catalyst to efficiently degrade chlorobenzene at a lower temperature of 240 °C, and minimized the production of chlorinated organic byproducts with the selectivity of HCl as high as almost 97 %. This work is of great significance for developing cheap and novel catalysts in chlorobenzene degradation while suppressing the secondary pollution of environment.

CRediT authorship contribution statement

Boqiong Jiang: Writing – review & editing, Resources, Project administration, Formal analysis, Conceptualization. **Yi Zhang:** Formal analysis, Data curation, Conceptualization. **Jingyi Han:** Formal analysis, Data curation, Conceptualization. **Yuhai Sun:** Writing – review & editing, Resources, Project administration, Formal analysis, Conceptualization. **Shaocai Yu:** Formal analysis, Data curation, Conceptualization. **Keyan Wei:** Formal analysis. **Jun Liu:** Writing – original draft, Methodology, Investigation, Formal analysis, Data curation, Conceptualization. **Xiaole Weng:** Formal analysis, Data curation, Conceptualization. **Hanfeng Lu:** Formal analysis, Data curation, Conceptualization.

Declaration of Competing Interest

The authors declare that they have no known competing financial interests or personal relationships that could have appeared to influence the work reported in this paper.

Acknowledgments

This work was supported by the National Natural Science Foundation of China (Grant NO. 52270109, 72361137007, 42175084), the Key Research and Development Program of Zhejiang Province (Grant NO. 2023C03127, 2024C03112). Zhejiang Gongshang University provincial colleges and universities basic research expenses (Grant NO. JRK23002, QRK23023). We also thank the support of Instrumental Analysis Center of Zhejiang Gongshang University.

Appendix A. Supporting information

Supplementary data associated with this article can be found in the online version at doi:10.1016/j.jhazmat.2024.136669.

Data availability

Data will be made available on request.

References

[1] Chai, S.H., Li, S.D., Li, W.M., Zheng, Q.Z., Wang, D.D., Chen, Y.F., 2022. Fabrication of high loading V_2O_5/TiO_2 catalysts derived from metal-organic framework with excellent activity for chlorobenzene decomposition. Appl Surf Sci 572, 151511. https://doi.org/10.1016/j.apsusc.2021.151511.

[2] Lin, F.W., Xiang, L., Zhang, Z.M., Li, N., Yan, B.B., He, C., et al., 2020. Comprehensive review on catalytic degradation of Cl-VOCs under the practical application conditions. Crit Rev Environ Sci Tec 52, 1–45. https://doi.org/10.1080/10643389.2020.1818490.

[3] Wang, T.J., Chen, T., Lin, X.Q., Zhan, M.X., Li, X.D., 2017. Emission and distribution of PCDD/Fs, chlorobenzenes, chlorophenols, and PAHs from stack gas of a fluidized bed and a stoker waste incinerator in China. Environ Sci Pollut Res 24 (6), 5607–5618. https://doi.org/10.1007/s11356-016-8221-9.

[4] Lin, F.W., Zhang, Z.M., Li, N., Yan, B.B., He, C., Hao, Z.P., et al., 2021. How to achieve complete elimination of Cl-VOCs: A critical review on byproducts formation and inhibition strategies during catalytic oxidation. Chem Eng J 404, 126534. https://doi.org/10.1016/j.cej.2020.126534.

[5] Zhang, J.J., Zhang, S.G., Liu, B., 2020. Degradation technologies and mechanisms of dioxins in municipal solid waste incineration fly ash: a review. J Clean Prod 250, 119507. https://doi.org/10.1016/j.jclepro.2019.119507.

[6] Wang, C., Tian, C.C., Guo, Y.L., Zhang, Z.D., Hua, W.C., Zhan, W.C., et al., 2018. Ruthenium oxides supported on heterostructured CoPO-MCF materials for catalytic oxidation of vinyl chloride emissions. J Hazard Mater 342, 290–296. https://doi.org/10.1016/j.jhazmat.2017.08.036.

[7] Guo, Y.L., Wen, M.C., Li, G.Y., An, T.C., 2021. Recent advances in VOC elimination by catalytic oxidation technology onto various nanoparticles catalysts: a critical review. Appl Catal B: Environ 281, 119447. https://doi.org/10.1016/j.apcatb.2020.119447.

[8] Du, C.C., Lu, S.Y., Wang, Q.L., Buekens, A.G., Ni, M.J., Debecker, D.P., 2018. A review on catalytic oxidation of chloroaromatics from flue gas. Chem Eng J 334, 519–544. https://doi.org/10.1016/j.cej.2017.09.018.

[9] Liu, X.L., Chen, L., Zhu, T.Y., Ning, R.L., 2019. Catalytic oxidation of chlorobenzene over noble metals (Pd, Pt, Ru, Rh) and the distributions of polychlorinated by-products. J Hazard Mater 363, 90–98. https://doi.org/10.1016/j.jhazmat.2018.09.074.

[10] Liang, W.J., Du, X.Y., Zhu, Y.X., Ren, S.D., Li, J., 2020. Catalytic oxidation of chlorobenzene over Pd-TiO_2/Pd-Ce/TiO_2 catalysts. Catalysts 10 (3), 347. https://doi.org/10.3390/catal10030347.

[11] Dai, Q., Bai, S., Wang, J., Li, M., Wang, X., Lu, G., 2013. The effect of TiO_2 doping on catalytic performances of Ru/CeO_2 catalysts during catalytic combustion of chlorobenzene. Appl Catal B: Environ 142-143, 222–233. https://doi.org/10.1016/j.apcatb.2013.05.026.

[12] Finocchio, E., Ramis, G., Busca, G., 2011. A study on catalytic combustion of chlorobenzenes. Catal Today 169 (1), 3–9. https://doi.org/10.1016/j.cattod.2010.10.097.

[13] Wu, M., Ung, K.C., Dai, Q.G., Wang, X.Y., 2012. Catalytic combustion of chlorinated VOCs over VO_x/TiO_2 catalysts. Catal Commun 18, 72–75. https://doi.org/10.1016/j.catcom.2011.11.028.

[14] Sun, W., Gong, B.W., Pan, J., Wang, Y.Y., Xia, H.Q., Zhang, H., et al., 2020. Catalytic combustion of CVOCs over Cr_xTi_{1-x} oxide catalysts. J Catal 391, 132–144. https://doi.org/10.1016/j.jcat.2020.08.007.

[15] Jiao, Y.M., Chen, X., He, F., Liu, S.T., 2019. Simple preparation of uniformly distributed mesoporous Cr/TiO_2 microspheres for low-temperature catalytic combustion of chlorobenzene. Chem Eng J 372, 107–117. https://doi.org/10.1016/j.cej.2019.04.118.

[16] Gu, Y.F., Cai, T., Gao, X.H., Xia, H.Q., Sun, W., Zhao, J., et al., 2019. Catalytic combustion of chlorinated aromatics over WO_x/CeO_2 catalysts at low temperature. Appl Catal B: Environ 248, 264–276. https://doi.org/10.1016/j.apcatb.2018.12.055.

[17] Yang, Y., Huang, J., Wang, S.W., Deng, S.B., Wang, B., Yu, G., 2013. Catalytic removal of gaseous unintentional POPs on manganese oxide octahedral molecular sieves. Appl Catal B: Environ 142-143, 568–578. https://doi.org/10.1016/j.apcatb.2013.05.048.

[18] Deng, W., Tang, Q.X., Huang, S.S., Zhang, L., Jia, Z.Y., Guo, L.M., 2020. Low temperature catalytic combustion of chlorobenzene over cobalt based mixed oxides derived from layered double hydroxides. Appl Catal B: Environ 278, 119336. https://doi.org/10.1016/j.apcatb.2020.119336.

[19] Yang, P., Yang, S.S., Shi, Z.N., Meng, Z.H., Zhou, R.X., 2015. Deep oxidation of chlorinated VOCs over CeO_2-based transition metal mixed oxide catalysts. Appl Catal B: Environ 162, 227–235. https://doi.org/10.1016/j.apcatb.2014.06.048.

[20] Feng, X.B., Tian, M.J., He, C., Li, L., Shi, J.W., Yu, Y.K., et al., 2020. Yolk-shell-like mesoporous $CoCrO_x$ with superior activity and chlorine resistance in dichloromethane destruction. Appl Catal B: Environ 264, 118493. https://doi.org/10.1016/j.apcatb.2019.118493.

[21] Fan, Y., Zhang, H.J., Ren, M.H., Zhang, Y.C., Li, Y., Wang, L.X., et al., 2021. Low-temperature catalytic degradation of chlorinated aromatic hydrocarbons over bimetallic Ce-Zr/UiO-66 catalysts. Chem Eng J 414, 128782. https://doi.org/10.1016/j.cej.2021.128782.

[22] Li, Y.X., Han, W., Wang, R.X., Weng, L.T., Serrano-Lotina, A., Bañares, M.A., et al., 2020. Performance of an aliovalent-substituted $CoCeO_x$ catalyst from bimetallic MOF for VOC oxidation in air. Appl Catal B: Environ 275, 119121. https://doi.org/10.1016/j.apcatb.2020.119121.
[23] Jiang, Y.W., Gao, J.H., Zhang, Q., Liu, Z.Y., Fu, M.L., Wu, J.L., et al., 2019. Enhanced oxygen vacancies to improve ethyl acetate oxidation over MnO_x-CeO_2 catalyst derived from MOF template. Chem Eng J 371, 78–87. https://doi.org/10.1016/j.cej.2019.03.233.
[24] Li, Z.J., Ma, C., Qi, M., Li, Y.L., Qu, Y.C., Zhang, Y., et al., 2023. CeO_2 from pyrolysis of MOFs for efficient catalytic combustion of VOCs. Mol Catal 535, 112857. https://doi.org/10.1016/j.mcat.2022.112857.
[25] Chen, X., Cai, S.C., Yu, E.Q., Chen, J., Jia, H.P., 2019. MnO_x/Cr_2O_3 composites prepared by pyrolysis of Cr-MOF precursors containing in situ assembly of MnO_x as high stable catalyst for toluene oxidation. Appl Surf Sci 475, 312–324. https://doi.org/10.1016/j.apsusc.2018.12.277.
[26] Li, G.B., Shen, K., Wang, L., Zhang, Y.P., Yang, H.Q., Wu, P., et al., 2021. Synergistic degradation mechanism of chlorobenzene and NO over the multi-active center catalyst: The role of NO_2, Brønsted acidic site, oxygen vacancy. Appl Catal B: Environ 286, 119865. https://doi.org/10.1016/j.apcatb.2020.119865.
[27] Qin, G.Z., Zheng, J.F., Li, Y.F., Yang, Y.T., Liu, X.M., Han, X.J., et al., 2022. Tailor the crystal planes of MIL-101(Fe) derivatives to enhance the activity of SCR reaction at medium and low temperature. J Colloid Interf Sci 615, 432–444. https://doi.org/10.1016/j.jcis.2022.01.147.
[28] Zheng, Y.F., Liu, Q.L., Shan, C.P., Su, Y., Fu, K.X., Lu, S.C., et al., 2021. Defective ultrafine MnO_x nanoparticles confined within a carbon matrix for low-temperature oxidation of volatile organic compounds. Environ Sci Technol 55 (8), 5403–5411. https://doi.org/10.1021/acs.est.0c08335.
[29] Li, X.H., Wang, J.J., Liu, X., Liu, L.M., Cha, D., Zheng, X.L., et al., 2019. Direct imaging of tunable crystal surface structures of MOF MIL-101 using high-resolution electron microscopy. J Am Chem Soc 141 (30), 12021–12028. https://doi.org/10.1021/jacs.9b04896.
[30] Zheng, Y.F., Fu, K.X., Yu, Z.H., Su, Y., Han, R., Liu, Q.L., 2022. Oxygen vacancies in a catalyst for VOCs oxidation: synthesis, characterization, and catalytic effects. J Mater Chem A 10 (27), 14171–14186. https://doi.org/10.1039/d2ta03180a.
[31] Cai, X., Zhang, Z.T., Cai, L.L., Tian, X.Y., Chu, W.D., Yang, W.S., 2022. Effect of calcination atmosphere on the structure and catalytic behavior of Cr_2O_3/Al_2O_3 catalysts for dehydrogenation of propane. Ind Eng Chem Res 61 (44), 16479–16488. https://doi.org/10.1021/acs.iecr.2c03031.
[32] Ma, Y., Wang, L., Ma, J.Z., Wang, H.H., Zhang, C.B., Deng, H., et al., 2021. Investigation into the enhanced catalytic oxidation of o-xylene over MOF-derived Co_3O_4 with different shapes: The role of surface twofold-coordinate lattice oxygen (O_{2f}). ACS Catal 11 (11), 6614–6625. https://doi.org/10.1021/acscatal.1c01116.
[33] Chen, X., Chen, X., Cai, S.C., Chen, J., Xu, W.J., Jia, H.P., et al., 2018. Catalytic combustion of toluene over mesoporous Cr_2O_3-supported platinum catalysts prepared by in situ pyrolysis of MOFs. Chem Eng J 334, 768–779. https://doi.org/10.1016/j.cej.2017.10.091.
[34] Lai, Y.T., Chen, T.C., Lan, Y.K., Chen, B.S., You, J.H., Yang, C.M., et al., 2014. Pt/SBA-15 as a highly efficient catalyst for catalytic toluene oxidation. ACS Catal 4 (11), 3824–3836. https://doi.org/10.1021/cs500733j.
[35] Xia, Y.S., Dai, H.X., Jiang, H.Y., Deng, J.G., He, H., Au, C.T., 2009. Mesoporous chromia with ordered three-dimensional structures for the complete oxidation of toluene and ethyl acetate. Environ Sci Technol 43, 8355–8360. https://doi.org/10.1021/es901908k.
[36] Zhou, G.L., He, X.L., Liu, S., Xie, H.M., Fu, M., 2015. Phenyl VOCs catalytic combustion on supported CoMn/AC oxide catalyst. J Ind Eng Chem 21, 932–941. https://doi.org/10.1016/j.jiec.2014.04.035.
[37] Zhang, L., He, D.D., Lu, J.C., Yan, J.L., Luo, Y.M., 2021. Catalytic properties and nature of active centers of Cr/MCM-41 in catalytic abatement of sulfur-containing VOC of methanethiol. Environ Technol Inno 24, 101975. https://doi.org/10.1016/j.eti.2021.101975.
[38] Su, J., Yao, W.Y., Liu, Y., Wu, Z.B., 2017. The impact of CrO_x loading on reaction behaviors of dichloromethane (DCM) catalytic combustion over Cr-O/HZSM-5 catalysts. Appl Surf Sci 396, 1026–1033. https://doi.org/10.1016/j.apsusc.2016.11.083.
[39] Yang, S., He, D.D., Zhang, L.M., Zhang, Y.L., Lu, J.C., Luo, Y.M., 2021. Toxic chromium treatment induce amino-assisted electrostatic adsorption for the synthesis of highly dispersed chromium catalyst. J Hazard Mater 417, 126155. https://doi.org/10.1016/j.jhazmat.2021.126155.
[40] Wang, J., Zhu, M.L., Song, Y.H., Liu, Z.T., Wang, L., Liu, Z.W., 2022. Molecular-level investigation on supported CrO_x catalyst for oxidative dehydrogenation of propane with carbon dioxide. J Catal 409, 87–97. https://doi.org/10.1016/j.jcat.2022.03.027.
[41] Li, X., Wang, S.W., Xu, B.K., Zhang, X., Xu, Y.H., Yu, P., et al., 2022. MOF etching-induced Co-doped hollow carbon nitride catalyst for efficient removal of antibiotic contaminants by enhanced perxymonosulfate activation. Chem Eng J 441, 136074. https://doi.org/10.1016/j.cej.2022.136074.
[42] Su, C.J., Li, Z., Mao, M.Q., Ye, W.H., Zhong, J.P., Ren, Q.M., et al., 2022. Unraveling specific role of carbon matrix over Pd/quasi-Ce-MOF facilitating toluene enhanced degradation. J Rare Earth 40 (11), 1751–1762. https://doi.org/10.1016/j.jre.2021.09.017.
[43] Guo, Z.Y., Lin, B.L., Huang, Y., Tang, J.L., Chen, P.R., Ye, D.Q., et al., 2024. Design of bimetallic catalyst with dual-functional Cu-Ce sites for synergistic NO_X and toluene abatement. Appl Catal B: Environ 342. https://doi.org/10.1016/j.apcatb.2023.123430.
[44] Chen, Y., Liao, Y.F., Chen, L., Chen, Z.F., Ma, X.Q., 2021. Performance of transition metal (Cu, Fe and Co) modified SCR catalysts for simultaneous removal of NO and volatile organic compounds (VOCs) from coal-fired power plant flue gas. Fuel 289, 119849. https://doi.org/10.1016/j.fuel.2020.119849.
[45] Liu, W.B., Zhou, J.B., Liu, D., Liu, S., Liu, X.J., Xiao, S., et al., 2021. Fe-MOF by ligand selective pyrolysis for Fenton-like process and photocatalysis: accelerating effect of oxygen vacancy. J Taiwan Inst Chem E 127, 327–333. https://doi.org/10.1016/j.jtice.2021.08.002.
[46] Huang, Q.L., Zhao, P.Z., Wang, W.W., Lv, L., Zhang, W.M., Pan, B.C., 2022. In situ fabrication of highly dispersed Co-Fe-doped-δ-MnO_2 catalyst by a facile redox-driving MOFs-derived method for low-temperature oxidation of toluene. ACS Appl Mater Interfaces 14 (48), 53872–53883. https://doi.org/10.1021/acsami.2c16620.
[47] Sun, Y.K., Xu, S., Bai, B., Li, L., Kang, Y., Hu, X.Q., et al., 2022. Biotemplate fabrication of hollow tubular $Ce_xSr_{1-x}TiO_3$ with regulable surface acidity and oxygen mobility for efficient destruction of chlorobenzene: Intrinsic synergy effect and reaction mechanism. Environ Sci Technol 56 (9), 5796–5807. https://doi.org/10.1021/acs.est.2c00270.
[48] Tsumori, N., Chen, L.Y., Wang, Q.J., Zhu, Q.L., Kitta, M., Xu, Q., 2018. Quasi-MOF: Exposing inorganic nodes to guest metal nanoparticles for drastically enhanced catalytic activity. Chem 4 (4), 845–856. https://doi.org/10.1016/j.chempr.2018.03.009.
[49] Wan, J., Yang, P., Guo, X.L., Zhou, R.X., 2019. Investigation on the structure-activity relationship of Nb_2O_5 promoting CeO_2-CrO_x-Nb_2O_5 catalysts for 1,2-dichloroethane elimination. Mol Catal 470, 75–81. https://doi.org/10.1016/j.mcat.2019.03.010.
[50] Yang, P., Shi, Z.N., Tao, F., Yang, S.S., Zhou, R.X., 2015. Synergistic performance between oxidizability and acidity/texture properties for 1,2-dichloroethane oxidation over $(Ce,Cr)_xO_2$/zeolite catalysts. Chem Eng Sci 134, 340–347. https://doi.org/10.1016/j.ces.2015.05.024.
[51] Ye, N., Li, Y., Yang, Z., Zheng, J., Zuo, S.F., 2019. Rare earth modified kaolin-based Cr_2O_3 catalysts for catalytic combustion of chlorobenzene. Appl Catal A, Gen 579, 44–51. https://doi.org/10.1016/j.apcata.2019.04.022.
[52] Dong, C., Qu, Z.P., Qin, Y., Fu, Q., Sun, H.C., Duan, X.X., 2019. Revealing the highly catalytic performance of spinel $CoMn_2O_4$ for toluene oxidation: involvement and replenishment of oxygen species using in situ designed-TP techniques. ACS Catal 9 (8), 6698–6710. https://doi.org/10.1021/acscatal.9b01324.
[53] Feng, C., Chen, C., Xiong, G.Y., Yang, D., Wang, Z., Pan, Y., et al., 2023. Cr-doping regulates Mn_3O_4 spinel structure for efficient total oxidation of propane: structural effects and reaction mechanism determination. Appl Catal B: Environ 328, 122528. https://doi.org/10.1016/j.apcatb.2023.122528.
[54] Tian, M.J., Guo, X., Dong, R., Guo, Z., Shi, J.W., Yu, Y.K., et al., 2019. Insight into the boosted catalytic performance and chlorine resistance of nanosphere-like meso-macroporous $CrO_x/MnCo_3O_x$ for 1,2-dichloroethane destruction. Appl Catal B: Environ 259, 118018. https://doi.org/10.1016/j.apcatb.2019.118018.
[55] Mo, S.P., Zhang, Q., Li, J.Q., Sun, Y.H., Ren, Q.M., Zou, S.B., et al., 2020. Highly efficient mesoporous MnO_2 catalysts for the total toluene oxidation: oxygen-vacancy defect engineering and involved intermediates using in situ DRIFTS. Appl Catal B: Environ 264, 118464. https://doi.org/10.1016/j.apcatb.2019.118464.
[56] Gopi, T., Swetha, G., Shekar, S.C., Ramakrishna, C., Gupta, A.K., 2017. Ozone assisted vapor phase selective catalytic oxidation of cyclohexane on the 13X zeolite supported cobalt oxides. J Environ Chem Eng 5 (4), 4031–4040. https://doi.org/10.1016/j.jece.2017.07.074.
[57] Chen, L., Liao, Y.F., Chen, Y., Wu, J.N., Ma, X.Q., 2020. Performance of Ce-modified V-W-Ti type catalyst on simultaneous control of NO and typical VOCS. Fuel Process Technol 207, 106483. https://doi.org/10.1016/j.fuproc.2020.106483.
[58] Zhao, S.Z., Wen, Y.F., Liu, X.J., Pen, X.Y., Lü, F., Gao, F.Y., et al., 2020. Formation of active oxygen species on single-atom Pt catalyst and promoted catalytic oxidation of toluene. Nano Res 13 (6), 1544–1551. https://doi.org/10.1007/s12274-020-2765-1.
[59] Gómez-Cazalilla, M., Infantes-Molina, A., Moreno-Tost, R., Maireles-Torres, P.J., Mérida-Robles, J., Rodríguez-Castellón, E., et al., 2009. Al-SBA-15 as a support of catalysts based on chromium sulfide for sulfur removal. Catal Today 143 (1-2), 137–144. https://doi.org/10.1016/j.cattod.2008.07.035.
[60] Zhang, X.J., Wei, Y.H., Song, Z.X., Liu, W., Gao, C.X., Luo, J.W., 2021. Silicotungstic acid modified CeO_2 catalyst with high stability for the catalytic combustion of chlorobenzene. Chemosphere 263, 128129. https://doi.org/10.1016/j.chemosphere.2020.128129.
[61] Sun, P.F., Wang, W.L., Dai, X.X., Weng, X.L., Wu, Z.B., 2016. Mechanism study on catalytic oxidation of chlorobenzene over $Mn_xCe_{1-x}O_2$/H-ZSM5 catalysts under dry and humid conditions. Appl Catal B: Environ 198, 389–397. https://doi.org/10.1016/j.apcatb.2016.05.076.
[62] Sun, B.H., Li, Q.Q., Su, G.J., Meng, B.W., Wu, M.G., Zhang, Q.F., et al., 2022. Insights into chlorobenzene catalytic oxidation over noble metal loading {001}-TiO_2: the role of $NaBH_4$ and subnanometer Ru undergoing stable $Ru^0 \leftrightarrow Ru^{4+}$ circulation. Environ Sci Technol 56 (22), 16292–16302. https://doi.org/10.1021/acs.est.2c05981.
[63] Liu, X.L., Zeng, J.L., Shi, W.B., Wang, J., Zhu, T.Y., Chen, Y.F., 2017. Catalytic oxidation of benzene over ruthenium–cobalt bimetallic catalysts and study of its mechanism. Catal Sci Technol 7 (1), 213–221. https://doi.org/10.1039/c6cy02141g.
[64] He, F., Jiao, Y.M., Wu, L.Y., Chen, X., Liu, S.T., 2019. Enhancement mechanism of Sn on the catalytic performance of Cu/KIT-6 during the catalytic combustion of chlorobenzene. Catal Sci Technol 9 (21), 6114–6123. https://doi.org/10.1039/c9cy01169b.
[65] Zhang, C., Zhang, J.P., Shen, Y.J., He, J.B., Qu, W.Q., Deng, J., et al., 2022. Synergistic catalytic elimination of NO_x and chlorinated organics: Cooperation of

acid sites. Environ Sci Technol 56 (6), 3719–3728. https://doi.org/10.1021/acs.est.1c08009.

[66] Lomnicki, S., Lichtenberger, J., Xu, Z., Waters, M., Kosman, J., Amiridis, M.D., 2003. Catalytic oxidation of 2,4,6-trichlorophenol over vanadia/titania-based catalysts. Appl Catal B: Environ 46 (1), 105–119. https://doi.org/10.1016/s0926-3373(03)00215-7.

[67] Zhang, Z.M., Xiang, L., Lin, F.W., Wang, Z., Yan, B.B., Chen, G.Y., 2021. Catalytic deep degradation of Cl-VOCs with the assistance of ozone at low temperature over MnO_2 catalysts. Chem Eng J 426, 130814. https://doi.org/10.1016/j.cej.2021.130814.

[68] Wang, X.W., Jiang, W.Y., Yin, R.Q., Sun, P.F., Lu, Y.H., Wu, Z.B., et al., 2020. The role of surface sulfation in mediating the acidity and oxidation ability of nickel modified ceria catalyst for the catalytic elimination of chlorinated organics. J Colloid Interf Sci 574, 251–259. https://doi.org/10.1016/j.jcis.2020.04.047.

[69] Hu, Z.Y., Chen, J., Yan, D.X., Li, Y., Jia, H.P., Lu, C.Z., 2021. Enhanced catalytic activities of MnO_x/Co_3O_4 nanocomposites prepared via MOFs-templated approach for chlorobenzene oxidation. Appl Surf Sci 551, 149453. https://doi.org/10.1016/j.apsusc.2021.149453.

[70] Weng, X.L., Xue, Y.H., Chen, J.K., Meng, Q.J., Wu, Z.B., 2020. Elimination of chloroaromatic congeners on a commercial V_2O_5-WO_3/TiO_2 catalyst: the effect of heavy metal Pb. J Hazard Mater 387, 121705. https://doi.org/10.1016/j.jhazmat.2019.121705.

[71] Weng, X.L., Sun, P.F., Long, Y., Meng, Q.J., Wu, Z.B., 2017. Catalytic oxidation of chlorobenzene over $Mn_xCe_{1-x}O_2$/HZSM-5 catalysts: a study with practical implications. Environ Sci Technol 51 (14), 8057–8066. https://doi.org/10.1021/acs.est.6b06585.

[72] Lichtenberger, J., Amiridis, M.D., 2004. Catalytic oxidation of chlorinated benzenes over V_2O_5/TiO_2 catalysts. J Catal 223 (2), 296–308. https://doi.org/10.1016/j.jcat.2004.01.032.

[73] Chen, L.Z., Liu, Y.J., Fang, X., Cheng, Y., 2021. Simple strategy for the construction of oxygen vacancies on α-MnO_2 catalyst to improve toluene catalytic oxidation. J Hazard Mater 409, 125020. https://doi.org/10.1016/j.jhazmat.2020.125020.